



Physical Conditions in the LMC's Quiescent Molecular Ridge: Fitting Non-LTE Models to CO Emission

Molly K. Finn¹ , Remy Indebetouw^{1,2} , Kelsey E. Johnson¹ , Allison H. Costa¹ , C.-H. Rosie Chen³ , Akiko Kawamura⁴ , Toshikazu Onishi⁵ , Jürgen Ott^{6,7} , Kazuki Tokuda^{4,5} , Tony Wong⁸ , and Sarolta Zahorecz^{4,5}

¹ Department of Astronomy, University of Virginia, Charlottesville, VA 22904, USA

² National Radio Astronomy Observatory, 520 Edgemont Road, Charlottesville, VA 22903, USA

³ Max-Planck-Institut für Radioastronomie, Auf dem Hügel 69, D-53121 Bonn, Germany

⁴ National Astronomical Observatory of Japan, National Institutes of Natural Sciences, 2-21-1 Osawa, Mitaka, Tokyo 181-8588, Japan

⁵ Department of Physical Science, Graduate School of Science, Osaka Prefecture University, 1-1 Gakuen-cho, Naka-ku, Sakai, Osaka 599-8531, Japan

⁶ National Radio Astronomy Observatory, P.O. Box O, Socorro, NM 87801, USA

⁷ Physics Department, New Mexico Institute of Mining and Technology, 801 Leroy Place, Socorro, NM 87801, USA

⁸ Astronomy Department, University of Illinois, 1002 W. Green Street, Urbana, IL 61801, USA

Received 2020 December 2; revised 2021 May 28; accepted 2021 June 6; published 2021 August 25

Abstract

The Molecular Ridge in the LMC extends several kiloparsecs south from 30 Doradus, and it contains $\sim 30\%$ of the molecular gas in the entire galaxy. However, the southern end of the Molecular Ridge is quiescent—it contains almost no massive star formation, which is a dramatic decrease from the very active massive-star-forming regions 30 Doradus, N159, and N160. We present new Atacama Large Millimeter/submillimeter Array and Atacama Pathfinder Experiment observations of the Molecular Ridge at a resolution as high as $\sim 16''$ (~ 3.9 pc) with molecular lines $^{12}\text{CO}(1-0)$, $^{13}\text{CO}(1-0)$, $^{12}\text{CO}(2-1)$, $^{13}\text{CO}(2-1)$, and $\text{CS}(2-1)$. We analyze these emission lines with our new multiline non-LTE fitting tool to produce maps of T_{kin} , n_{H_2} , and N_{CO} across the region based on models from RADEX. Using simulated data for a range of parameter space for each of these variables, we evaluate how well our fitting method can recover these physical parameters for the given set of molecular lines. We then compare the results of this fitting with LTE and X_{CO} methods of obtaining mass estimates and how line ratios correspond with physical conditions. We find that this fitting tool allows us to more directly probe the physical conditions of the gas and estimate values of T_{kin} , n_{H_2} , and N_{CO} that are less subject to the effects of optical depth and line-of-sight projection than previous methods. The fitted n_{H_2} values show a strong correlation with the presence of young stellar objects (YSOs), and with the total and average mass of the associated YSOs. Typical star formation diagnostics, such as mean density, dense gas fraction, and virial parameter do not show a strong correlation with YSO properties.

Unified Astronomy Thesaurus concepts: Star formation (1569); Large Magellanic Cloud (903); Molecular clouds (1072); Millimeter astronomy (1061); Interstellar medium (847)

1. Introduction

Our understanding of star formation is heavily dependent on our understanding of molecular clouds and the physics that governs them. It is difficult, and in many cases impossible, to determine those physical conditions without relying on assumptions or scaling relations (e.g., Kennicutt 1998). These assumptions appear to be sufficient in many cases, but there are examples of clouds and regions of galaxies that are not forming stars as we would expect based on these scaling relations. For example, “Maddalena’s Cloud” G126-2.5 is a giant molecular cloud in the Milky Way that has unusually low star formation (Maddalena & Thaddeus 1985), and the star formation rate in the Central Molecular Zone in the Galactic Center is an order of magnitude lower than would be predicted by Galactic trends (Longmore et al. 2013). To understand why, we must determine physical conditions without making assumptions that molecular clouds are behaving in the “typical” way.

One of the most common mass estimates for molecular clouds comes from the CO-to- H_2 conversion factor, X_{CO} , which is discussed in detail in Bolatto et al. (2013). It is often calibrated with the virial mass or dust mass and is used to convert the integrated intensity of $^{12}\text{CO}(1-0)$ emission to a column density of H_2 . The X_{CO} factor method is most valid when determining masses on large size scales where many

molecular clouds are smoothed together, averaging over the varying physical conditions. On the scale of individual star-forming clouds or individual lines of sight, the conversion of CO flux to H_2 column density with an adopted X_{CO} factor cannot be expected to be constant (Bolatto et al. 2013, and references therein).

Another measure of mass can be made by assuming local thermal equilibrium (LTE) to get excitation temperature, optical depth, and column density (Mangum & Shirley 2015). This method is based on the assumption that the gas is sufficiently dense for the molecular excitation levels to have a Boltzmann distribution corresponding to an excitation temperature, T_{ex} , and that the excitation temperatures of ^{12}CO and ^{13}CO are equal. This method also often assumes that ^{12}CO is optically thick, allowing for an easy estimate of the excitation temperature (T_{ex}) from the brightness temperature (T_{B}), while ^{13}CO is optically thin, which makes it possible to determine the optical depth with an assumption of the relative abundance of ^{12}CO and ^{13}CO (Koeppen & Kegel 1980).

However, these calculations break down if ^{12}CO becomes optically thin, or if either line’s level population is not well described by a Boltzmann distribution. Studies have shown regimes in which the LTE calculations overestimate the column density by up to a factor of two in bright ($T_{\text{B}} > 40$ K) clouds (Indebetouw et al. 2020), and underestimate the mass by up to a

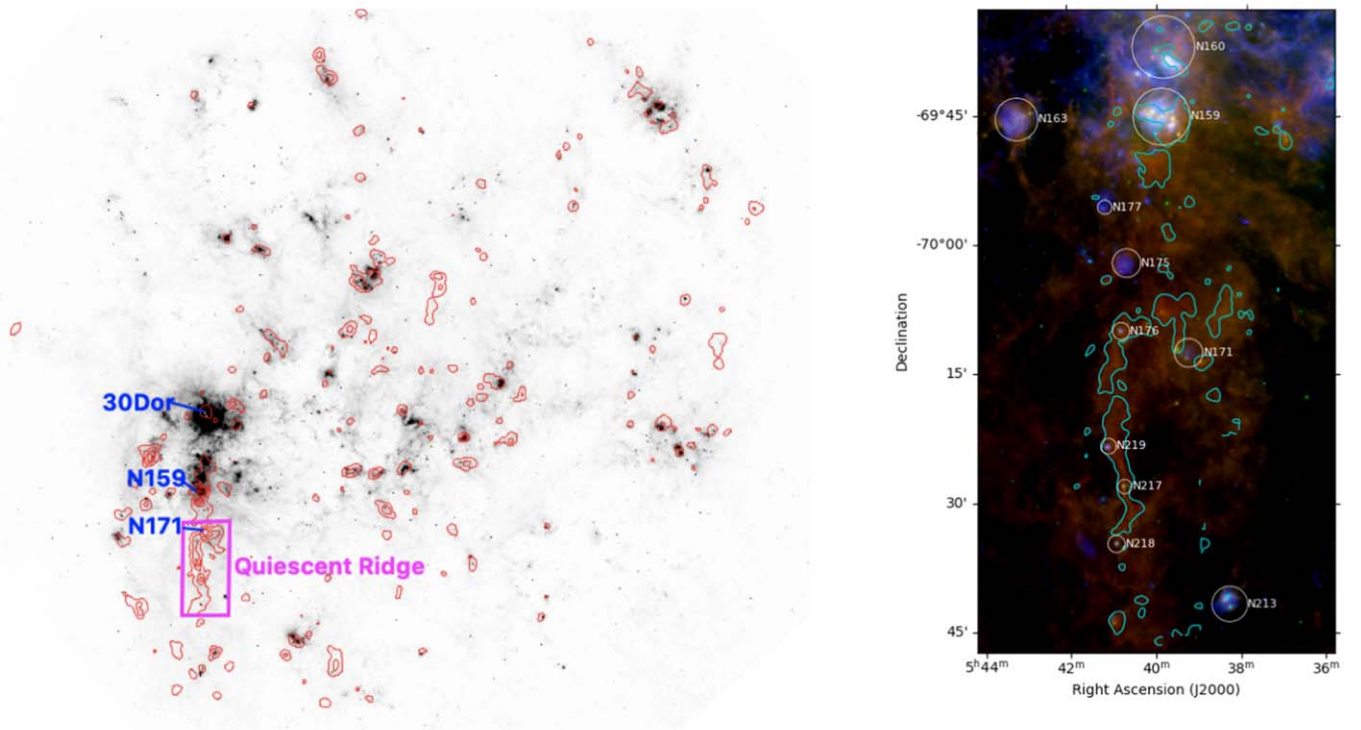


Figure 1. Left: the LMC with the Molecular Ridge highlighted in pink and active star-forming regions 30 Doradus (30 Dor), N159, and N171 in blue. The grayscale is Multiband Imaging Photometer for Spitzer (MIPS) $24\ \mu\text{m}$ from the SAGE survey (Meixner et al. 2006), and the red contours are $^{12}\text{CO}(1-0)$ from the NANTEN survey (Fukui et al. 2008). We can see from this that the Ridge is a unique feature, showing up prominently in the red $^{12}\text{CO}(1-0)$ contours, but lacking any strong emission in the $24\ \mu\text{m}$ grayscale, which is a common star formation tracer. Right: three-color image zoomed in on the Ridge. The red is Photodetector Array Camera and Spectrometer (PACS) $250\ \mu\text{m}$ from the HERITAGE survey, green is the same $24\ \mu\text{m}$ as the grayscale on the left, and blue is $\text{H}\alpha$ from the Magellanic Cloud Emission Line (MCELS) survey (Smith & MCELS Team 1998). The cyan contours are $^{12}\text{CO}(1-0)$ from the Magellanic Mopra Assessment (MAGMA) survey, and H II regions identified by Henize (1956) are shown as white circles.

factor of seven when the ^{13}CO becomes sub-thermally excited (Castets et al. 1990; Padoan et al. 2000; Heyer & Dame 2015). The assumption of LTE also requires that the density of the gas is sufficiently high such that the excitation is entirely governed by temperature, meaning that any dependence on density drops out of the equations and so cannot be solved for.

Ratios of isotopologues (e.g., $^{13}\text{CO}/^{12}\text{CO}$) can trace volume density in the case where one line is optically thick and the other line is sub-thermally excited (Nishimura et al. 2015). Ratios of upper to lower excitation levels of CO (e.g., $^{12}\text{CO}(2-1)/^{12}\text{CO}(1-0)$) scale with excitation temperature and density when both lines are optically thin, and the ratio approaches unity as the lines get increasingly optically thick (Sakamoto 1994; Nishimura et al. 2015; Peñaloza et al. 2017). These ratios are also dependent on optical depth and local abundance ratios and so can only provide rough diagnostics of the density and temperature (Peñaloza et al. 2017).

In this study, we fit molecular line observations to the results of non-LTE escape probability models from RADEX (van der Tak et al. 2007). This avoids many of the assumptions required for other methods, such as those listed above, and so allows us to better characterize the actual physical conditions of the gas. With this method, we obtain estimates of not just the temperature and column density, but also the volume density. Our only assumptions in this case are that the different molecular lines are tracing the same gas with a constant abundance ratio throughout the cloud, and that the gas in each voxel is homogeneous—we fit only one set of physical conditions for each pixel and velocity channel despite the fact

that temperature and density almost certainly vary along the line of sight and within the beam. Through this model-fitting study, we determine the physical conditions of molecular clouds in the Large Magellanic Cloud (LMC) and compare those results to other common methods: adopting an X_{CO} factor, assuming LTE, or using line diagnostics.

We use as a case study the quiescent southern end of the Molecular Ridge in the LMC, extending 1–2 kpc south from 30 Doradus (Figure 1). We assume a distance to the LMC of 50 kpc (Schaefer 2008). Cohen et al. (1988) first noted the Ridge as a striking feature in low-resolution maps of $^{12}\text{CO}(1-0)$, and further observations of ^{12}CO by the NANTEN survey (Fukui et al. 2008) revealed that it contained $\sim 30\%$ of all CO-bright molecular gas mass in the LMC (Mizuno et al. 2001). Despite the large reservoir of molecular gas, the Ridge is surprisingly quiescent, showing little sign of star formation based on the presence of young optical clusters or $\text{H}\alpha$ emission (Davies et al. 1976; Bica et al. 1996; Yamaguchi et al. 2001). Indebetouw et al. (2008) found the $\text{H}\alpha$ emission (Calzetti et al. 2007) would predict a star formation rate of $2.6 \times 10^{-4} M_{\odot} \text{ yr}^{-1}$, while the star formation rate predicted by the molecular gas surface density and the Schmidt–Kennicutt law (Kennicutt 1998) would be $8 \times 10^{-3} M_{\odot} \text{ yr}^{-1}$, over a factor of 30 larger. There are only five H II regions in the Ridge that were identified and named by Henize (1956), most notably N171, as well as some fainter H II regions (see Figure 1).

By looking for embedded stellar objects in the Ridge from the Spitzer “Surveying the Agents of a Galaxy’s Evolution” (SAGE) survey (Meixner et al. 2006), Indebetouw et al. (2008)

Table 1
Observations Used in This Analysis

Source	Line	Beam ($''$)	RMS (K)	Velocity Channel
ALMA ACA	$^{13}\text{CO}(1-0)$	16	0.033	0.5 km s^{-1}
ALMA ACA	CS(2-1)	18	0.025	0.5 km s^{-1}
ALMA TP	$^{13}\text{CO}(1-0)$	63	0.0078	0.19 km s^{-1}
ALMA TP	CS(2-1)	70	0.0062	0.19 km s^{-1}
MAGMA	$^{12}\text{CO}(1-0)$	45	0.11	0.5 km s^{-1}
APEX	$^{12}\text{CO}(2-1)$	29	0.23	1.0 km s^{-1}
APEX	$^{13}\text{CO}(2-1)$	30	0.065	1.0 km s^{-1}

showed that the lack of young, blue clusters and low H α emission is likely due to the Ridge preferentially forming relatively low-mass star clusters rather than having deeply embedded high-mass objects or simply not forming stars at all (the star formation measured by modeling the young stellar object (YSO) population was a factor of two lower than that predicted from the extragalactic Schmitt–Kennicutt law, Kennicutt 1998, but agreed within the uncertainties). This is a stark contrast to 30 Doradus and the active massive star formation regions N159 and N160 directly to the north of the Ridge that are forming massive stars prodigiously. This makes the Molecular Ridge a particularly interesting region for studies of the molecular gas properties.

The quiescence of the Ridge could be due to atypical gas conditions, so a robust, assumption-minimizing approach is needed to analyze its physical conditions. To do this, we use four molecular lines— $^{12}\text{CO}(1-0)$, $^{13}\text{CO}(1-0)$, $^{12}\text{CO}(2-1)$, and $^{13}\text{CO}(2-1)$, the observations of which are described in Section 2. We fit non-LTE RADEX models to those observed lines as described in Section 3, and so avoid assumptions about stability, local excitation, or optical depth. We evaluate the performance of this fitting and details of methodology choices in Appendices A–C.

In Section 4, we segment the emission into clumps and determine the physical properties of these clumps. We then discuss YSOs detected in the Ridge and match them to those CO clumps in Section 5. We evaluate how the derived properties of the clumps compare with other common methods of determining physical conditions in Section 6, and how the derived properties correlate with star formation as traced by the presence of associated YSOs in Section 7. Our major results are summarized in Section 8.

2. Observations

In this analysis, we make use of new $^{13}\text{CO}(1-0)$ and CS(2-1) data from the Atacama Large Millimeter/submillimeter Array (ALMA) 7 m Atacama Compact Array (ACA), described in Section 2.1. We also use $^{12}\text{CO}(1-0)$ data from the Mopra Telescope taken as part of the Magellanic Mopra Assessment (MAGMA) survey (Wong et al. 2011), and new observations of $^{12}\text{CO}(2-1)$ and $^{13}\text{CO}(2-1)$ from the Atacama Pathfinder Experiment (APEX), described in Section 2.2. These observations are summarized in Table 1, and the integrated intensity maps are shown in Figure 2. The errors reported in Table 1 are the rms noise in line-free regions of the data cubes in a single channel of 1 km s^{-1} . Though Table 1 and Figure 2 show the resolutions obtained for each set of observations, the majority of the analysis presented in this paper is performed with all data sets convolved to $45''$ and 1.0 km s^{-1} velocity resolution to

compare among the data sets. The final data cubes used in the analysis are available as supplementary material.⁹

2.1. ALMA Data

Interferometric data were obtained in three maps with the ALMA 7 m ACA for project 2017.1.00271.S. The data contain three spectral windows centered on $^{13}\text{CO}(1-0)$, C $^{18}\text{O}(1-0)$, and CS(2-1), each with 2048 61.035 kHz channels (125 MHz bandwidth). An additional 2 GHz wide spectral window with coarse channels (0.98 MHz) was observed centered on H40 α at 99 GHz. The northwest 96-pointing map was observed nine times between 2017 November 7 and 2017 November 15 for a total of 438 minutes on source. J0522-3627 (5–5.5 Jy) and J0529-7245 (600–700 mJy) were used for bandpass and amplitude, and for phase calibration, respectively. The central 76-pointing map was observed nine times between 2017 October 15 and 2017 November 6 for a total of 346 minutes on source, and the southern 106-pointing map 11 times between 2017 October 15 and 2017 November 6 for a total of 470 minutes on source. Those maps used the same bandpass and amplitude calibrator as the northern. In a given execution, either J0635-7516 (1.25 Jy) or J0529-7245 was used for phase calibration.

The data were calibrated with the ALMA data pipeline Pipeline-CASA51-P2-B, v.40896¹⁰ (L. Davis 2022, in preparation), packaged with CASA 5.1.1-5¹¹ (McMullin et al. 2007). The standard pipeline recipe and default parameters were used as described in the ALMA pipeline User’s Guide. Visibilities are calibrated at full spectral resolution. Time-varying gains are solved on the phase calibrator using the 2 GHz wide spectral window, and transferred to the narrow spectral windows using a constant spw–spw phase offset during each 1.5 hr execution block. Gains are transferred to the science target on the scan timescale with linear interpolation in time. Weights are set correctly by the ALMA correlator and propagated through the calibration process, so no statwt is required. Continuum and line spectral channels are found in each spectral window by the pipeline task findCont described in the manual. A linear per-visibility fit is performed and subtracted in the uv domain. The pipeline images data at full spectral resolution, but we re-imaged the calibrated continuum-subtracted visibilities as described below.

By design, project 2017.1.00271.S did not cover the $\sim 2'$ H II region at 5:39:50–70:08:00 because it was already observed with ALMA ACA by projects 2012.1.00603.S and 2015.1.00196.S. These projects also have three narrow spectral windows centered on $^{13}\text{CO}(1-0)$, C $^{18}\text{O}(1-0)$, and CS(2-1), and a 2 GHz wide spectral window. The narrow windows have 30.518 kHz and 122.07 kHz channels in 2012.1.00603.S and 2015.1.00196.S, respectively, but all have 125 MHz bandwidth like the primary dataset. The wide window is centered at 96.8 GHz in project 2015.1.00196.S, but that spectral window is not analyzed here. Project 2012.1.00603.S was observed eight times between 2013 December 17 and 2015 April 28, using Ganymede, J0519-4546 (1.3 Jy), Uranus, Callisto, or Mars as the amplitude calibrator, J0538-4405, J0519-4546, J0635-7516, or J1037-2934 as the bandpass calibrator, and J0635-7516 or J0601-7036 as the phase calibrator. Those data

⁹ <https://doi.org/10.5281/zenodo.4838414>

¹⁰ <https://almascience.nrao.edu/processing/>

¹¹ casa.nrao.edu

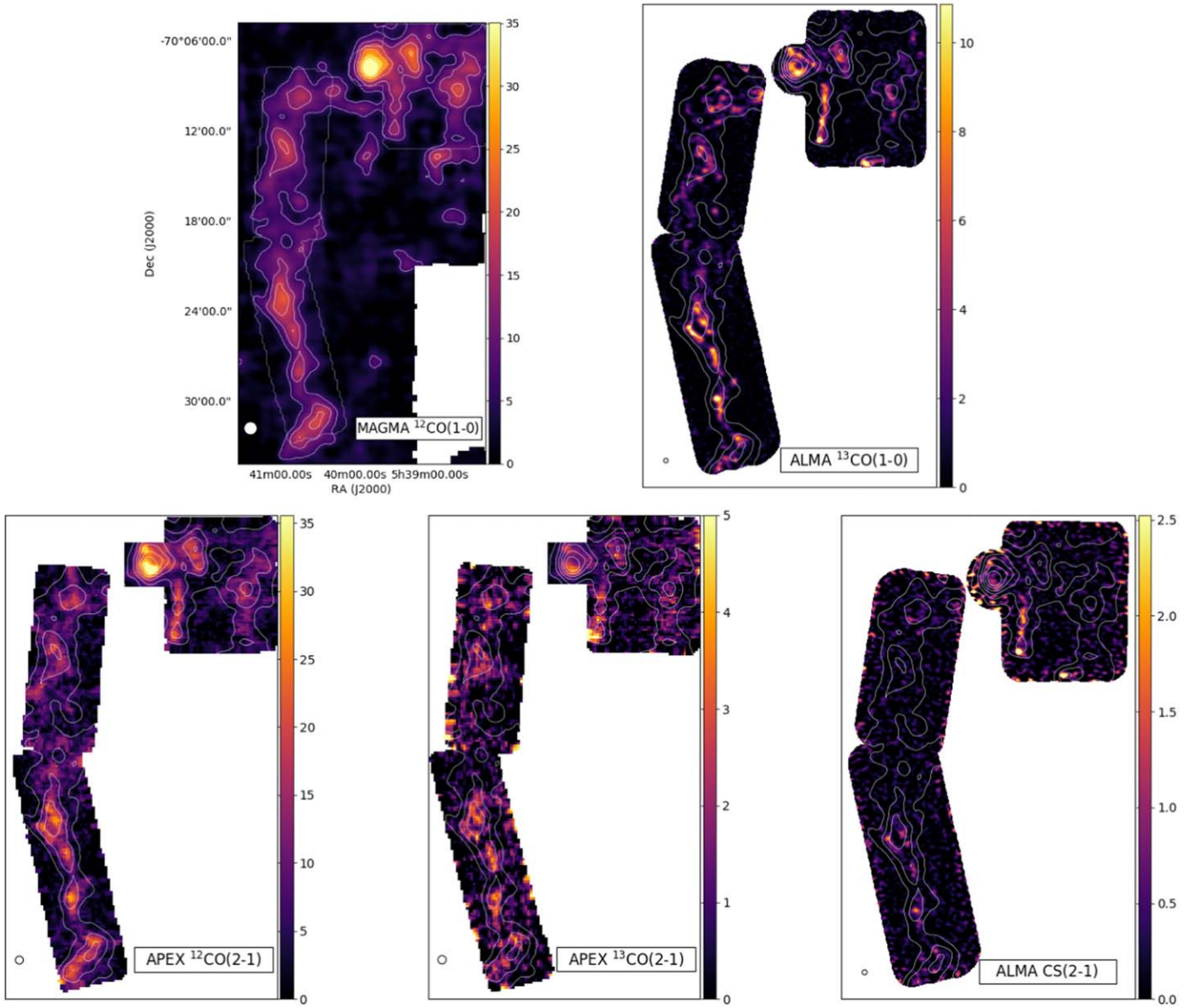


Figure 2. Integrated intensity maps of the observations used in this analysis. The contours are the integrated intensity of $^{12}\text{CO}(1-0)$ at intervals of 6, 12, 18, 24, and 30 K km s^{-1} . The dotted contour in the MAGMA $^{12}\text{CO}(1-0)$ map shows the common observational footprint of all of the maps. All maps are in units of K km s^{-1} , and the beams are shown in the lower left corners.

were calibrated manually by ALMA staff, using a script accessible in the ALMA archive. That script solves for time-varying gains on each spectral window individually, and transfers the gains from phase calibrator to science target, but not between spectral windows.

Project 2015.1.00196.S was observed eight times between 2016 May 1 and 2016 June 12, using J0538-4405 (2.6 Jy) or J1107-4449 (1.3 Jy) for bandpass calibration, J0538-4405 or Uranus for amplitude calibration, and J0529-7245 (700–850 mJy) for phase calibration. The data were calibrated with Pipeline-CASA56-P1-B v.42866 packaged with CASA 5.6.1-8, following the same procedure as the primary dataset 2017.1.00271.S.

There were no detections in $\text{C}^{18}\text{O}(1-0)$ above a 3σ upper limit of 200 mJy. The $^{13}\text{CO}(1-0)$ visibility data from 2012.1.00603.S and the CS(2-1) data from 2012.1.00603.S and 2015.1.00196.S were added to the 2017.1.00271.S NW tile data before imaging.

For all projects, total power ALMA data was obtained for rectangular regions corresponding to the interferometric maps, extended by one primary beam in both dimensions. Project 2012.1.00603.S was observed four times between 2013 December 16 and 2014 December 14, and processed with Pipeline-Cycle2-R1-B v.31667 in CASA 4.2.2. Project 2015.1.00196.S was observed 13 times between 2016 March 23 and 2016 April 8 and processed with Pipeline-Cycle3-R4-B v.36660 in CASA 4.5.3. Project 2017.1.00271.S NW, central, and southern maps were observed 23 times between 2018 March 30 and 2018 April 23, 25 times between 2018 January 9 and 2018 April 5, and 22 times between 2018 January 24 and 2018 March 21, respectively. All 2017.1.00271.S data were calibrated and imaged with Pipeline-CASA51-P2-B v.40896 packaged with CASA 5.1.1-5. The ALMA single dish pipeline is also described in the user’s manual, and the standard procedure was used: application of system temperature amplitude calibration, subtraction of an off position, line

detection by clustering analysis, fitting and removal of a polynomial baseline, and a second iteration of line detection and baseline removal. The spectra are then gridded to produce image cubes at native spectral resolution, with beams and rms as noted in Table; 1.

The interferometric data were imaged and combined with the total power data using CASA 5.6.1–8. For the line cubes, total power images were Hanning smoothed and used as a starting model for interferometric deconvolution with the `tclean` task. The images have a cell size of $2''.1 \times 2''.1 \times 0.5 \text{ km s}^{-1}$, were cleaned to a 1σ threshold (0.6 Jy/bm for $^{13}\text{CO}(1-0)$ and 0.3 Jy/bm for $\text{CS}(2-1)$) using the mosaic gridded, hogbom deconvolver, briggs weighting with `robust`=0.5, and auto-multithresh masking using the pipeline default automasking parameters. Use of the total power starting model increases the signal-to-noise on the “overlap” spatial scales to which the interferometric and total power are both sensitive, but can overestimate the total flux density after nonlinear deconvolution. To correct the flux, the final deconvolved image is combined with the total power image (multiplied by the interferometric sensitivity map) using the `feather` task, which adds the two images in the Fourier domain and ensures the correct total flux density on all spatial scales. The interferometer recovered 40% of the total flux across the region, with individual clouds recovering between 15% and 99%. The final combined image is then divided by the interferometric sensitivity map to obtain the correct flux scale as a function of position. We then convolved the three regions to a common circular beam of $16''.0$ and $18''.2$ for $^{13}\text{CO}(1-0)$ and $\text{CS}(2-1)$, respectively, and mosaicked them into a single map, linearly weighted by each tile’s sensitivity image.

2.2. APEX Data

$^{12}\text{CO}(2-1)$ and $^{13}\text{CO}(2-1)$ were observed with the APEX 12m telescope between 2017 August 14 and 24, under project No. 0100.F-9313(A). The observations were taken with the APEX-1 receiver, resulting in a beam size of $27''.8$ – $29''.0$. Three maps were obtained, corresponding to the three ALMA maps, using on-the-fly mapping. Standard calibration was performed using R-Dor, Venus, RAFGL1235, and 07454-7112. Data reduction was carried out using GILDAS/CLASS; to increase the signal-to-noise ratios in individual channels, contiguous channels were smoothed to a velocity resolution of 1.0 km s^{-1} and then baseline subtracted, resulting in rms ~ 0.24 and 0.09 K for ^{12}CO and ^{13}CO , respectively. The APEX data cubes were gridded to $9'' \times 9''$ (~ 3 pixels per beam) to facilitate comparisons with the ALMA data cubes. As with the interferometric ALMA data, the $2'$ region at 5:39:50–70:08:00 was not observed with APEX, but instead, the archival ALMA total power data for $^{12}\text{CO}(2-1)$ and $^{13}\text{CO}(2-1)$ from projects 2012.1.00603.S and 2015.1.00196.S were added to our APEX mosaic. The APEX and ALMA images were combined after convolving the images to a common beam size and gridding as an average weighted by each image’s sensitivity map.

3. Radex Fitting

3.1. Fitting Method

To determine physical parameters from the observed ^{12}CO and ^{13}CO emission lines, we compared the line intensities at each pixel and velocity to model intensities for a range of physical parameters from the non-LTE escape probability code

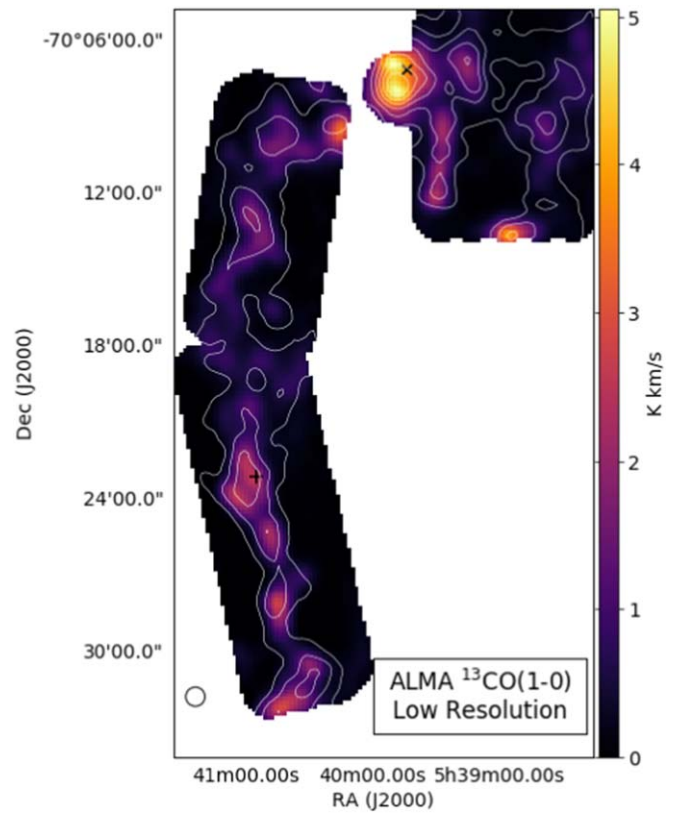


Figure 3. Integrated intensity map of $^{13}\text{CO}(1-0)$ convolved to a resolution of $45''$ (beam shown in lower left corner) to match the limiting resolution of the $^{12}\text{CO}(1-0)$ map. The contours are the integrated intensity of $^{12}\text{CO}(1-0)$ as shown in Figure 2, and locations of the example spectra shown in Figure 4 are marked with a cross for panel (a) and an “X” for panel (b). The majority of the analysis in this paper is performed at this lowered resolution, including the RADEX fitting.

RADEX (van der Tak et al. 2007). This was done by computing a three-dimensional grid of RADEX models for a range of kinetic temperatures (T_{kin}), H_2 volume densities (n_{H_2}), and ^{12}CO column densities (N_{CO}). The four emission cubes— $^{12}\text{CO}(1-0)$, $^{13}\text{CO}(1-0)$, $^{12}\text{CO}(2-1)$, and $^{13}\text{CO}(2-1)$ —were all convolved to $45''$ and 1 km s^{-1} to match the lowest common resolutions among the data sets. The errors used in calculating probabilities are the rms errors in these newly convolved maps, measured in emission-free slices of the cubes. The lower-resolution errors for $^{12}\text{CO}(1-0)$, $^{13}\text{CO}(1-0)$, $^{12}\text{CO}(2-1)$, and $^{13}\text{CO}(2-1)$ are 0.11 K , 0.017 K , 0.1 K , and 0.035 K , respectively. We show the $^{13}\text{CO}(1-0)$ map at this lowered resolution in Figure 3 and example input spectra for the lines in Figure 4.

When computing RADEX models, we used a homogeneous spherical escape probability geometry with a line width of 1 km s^{-1} to match our observations’ velocity channels, and a background temperature of 2.73 K . We also assume that the ratio of ^{12}CO to ^{13}CO (R_{13}) is in the range 50–100 (Nikolić et al. 2007) and that $N_{^{12}\text{CO}}/N_{^{13}\text{CO}} = R_{13}$.

We limited the ranges of the parameters to be T_{kin} between 2 and 200 K , n_{H_2} between $10^{1.5}$ and 10^7 cm^{-3} , and N_{CO} between 10^{14} and 10^{18} cm^{-2} . The ranges of n_{H_2} and N_{CO} are evenly spaced in log space, T_{kin} is spaced linearly. When computing the RADEX grid, we also excluded regions of the parameter space where RADEX predictions are less reliable, such as where the optical depth gets very large ($\tau > 300$), where ^{12}CO becomes overpopulated and the excitation gets inflated

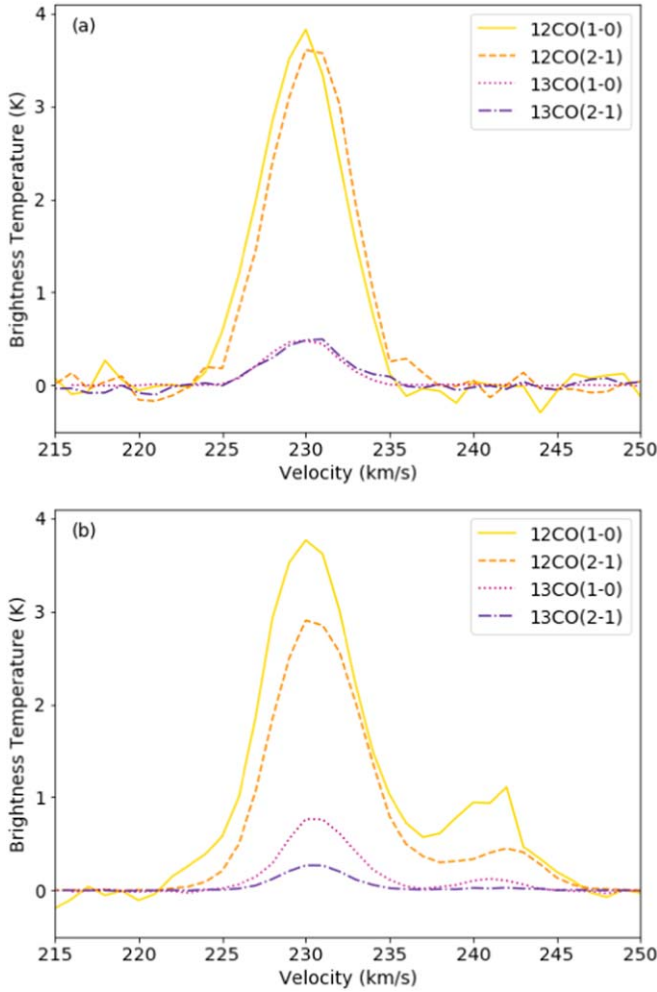


Figure 4. Example spectra of $^{12}\text{CO}(1-0)$, $^{12}\text{CO}(2-1)$, $^{13}\text{CO}(1-0)$, and $^{13}\text{CO}(2-1)$ from two different peaks. These are examples of spectra that are used in the RADEX fitting, and so are taken from maps that have all been convolved to a beam size of $45''$. The top panel shows a spectra that is typical throughout the region, while the bottom panel shows an example with more velocity structure from the northern region of the map. The locations of these two spectra are shown in the $^{13}\text{CO}(1-0)$ map in Figure 3.

($T_{\text{ex}} > 2.5 \times T_{\text{kin}}$; Koeppen & Kegel 1980), where any output values become unphysically negative, and where RADEX took more than 999,000 iterations to solve.

For each combination of the three parameters, $\mathbf{p} = (T_{\text{kin}}, n_{\text{H}_2}, N_{\text{CO}})$, the resultant model brightness temperatures from RADEX, $R(\mathbf{p})$, and the beam filling factor, f , were used to compute a probability given the observed brightness temperature for some voxel, I , and its error, δ , for each observed line, j , using the equation

$$P(\mathbf{p}|I) = \prod_j \frac{-1}{\delta_j} \exp \left[\frac{1}{2} \left(\frac{(I_j - R(\mathbf{p})_j \times f)}{\delta_j} \right)^2 \right]. \quad (1)$$

We find the combination of parameter values that yields the greatest probability, \mathbf{p}_{max} . We then find the odds ratio for all other parameter combinations in the grid:

$$O = \frac{P(\mathbf{p}_{\text{max}}|I)}{P(\mathbf{p}|I)}. \quad (2)$$

In the case of uniform priors (so $P(\mathbf{p}_{\text{max}}) = P(\mathbf{p})$, which we assume here for all parameters), this reduces to the Bayes

factor:

$$B = \frac{P(I|\mathbf{p}_{\text{max}})}{P(I|\mathbf{p})}. \quad (3)$$

To compare \mathbf{p}_{max} with all other combinations of parameters, we use the “Jeffreys” scale (Trotta 2008) to determine if \mathbf{p}_{max} is “inconclusively,” “weakly,” “moderately,” or “strongly” preferred to the other parameter combinations. Trotta (2008) defines this empirically derived scale as follows: a value of $|\ln B| < 1$ corresponds to inconclusive evidence, $1 \leq |\ln B| < 2.5$ is weak evidence, $2.5 \leq |\ln B| < 5$ is moderate evidence, and $|\ln B| \geq 5$ is strong evidence. The value of $|\ln B|$ is zero for \mathbf{p}_{max} , and increases for parameter combinations that have lower probabilities of matching the observed intensities.

After excluding the regions of parameter space for which $|\ln B| \geq 5.0$ (\mathbf{p}_{max} is strongly preferred over all of the excluded parameter combinations), we determine the ranges of the remaining parameter space for each parameter to obtain what we call here “Bayesian intervals.” We do the same to get intervals excluding parameter combinations with $|\ln B| \geq 2.5$ and $|\ln B| \geq 1.0$ to get intervals outside of which \mathbf{p}_{max} is “moderately” and “weakly” preferred, respectively. In this case, the “strong” 5.0 Bayesian interval is the largest and least constrained of the three, since parameter combinations in which \mathbf{p}_{max} is only moderately or weakly preferred are included within the interval. The “weak” 1.0 Bayesian interval is the narrowest and most constrained, since \mathbf{p}_{max} only needs to be weakly preferred over a parameter combination for it to be excluded.

The Bayesian intervals and \mathbf{p}_{max} all depend entirely on the three-dimensional probability density function (PDF). In addition to these intervals, we also consider each individual parameter’s probability density profile, integrated over the other two parameters. From these profiles, we determine 1σ and 2σ (67% and 95%, respectively) confidence intervals, defined as the smallest ranges of the parameters for which the sum under their normalized probability profiles is 0.67 and 0.95, respectively. The confidence intervals depend only on the integrated one-dimensional profiles instead of the three-dimensional PDF and therefore depend on the spacing of intervals used in the parameter ranges. Since the n_{H_2} and N_{CO} ranges span several orders of magnitude, the confidence intervals are determined in log space so as not to overly weight the higher values. The confidence interval of T_{kin} is calculated with linear spacing.

An example corner plot showing a resultant distribution for one pixel of data is shown in Figure 5. The profiles along the diagonal show some of the metrics described above: \mathbf{p}_{max} , the collapsed one-dimensional probability profiles, and the two smallest Bayesian intervals.

We attempted to independently constrain R_{13} in the same way as the other parameters, adding it as a fourth dimension to the tested parameter space. However, R_{13} was rarely constrained, and including it significantly increased the computational requirements. We therefore assumed a range of $R_{13} = 50$ –100 instead (Nikolić et al. 2007) and performed the fitting once with $R_{13} = 50$ and once with $R_{13} = 100$. With additional observations of higher J ^{12}CO and ^{13}CO lines, we might be able to constrain R_{13} on a pixel-by-pixel basis, making it worth the additional computational requirements.

We similarly attempted to include fitting the beam filling factor as a fourth parameter with minimal success. Appendix A goes into detail about the various attempts at fitting and measuring the beam filling factor. After examining the results of

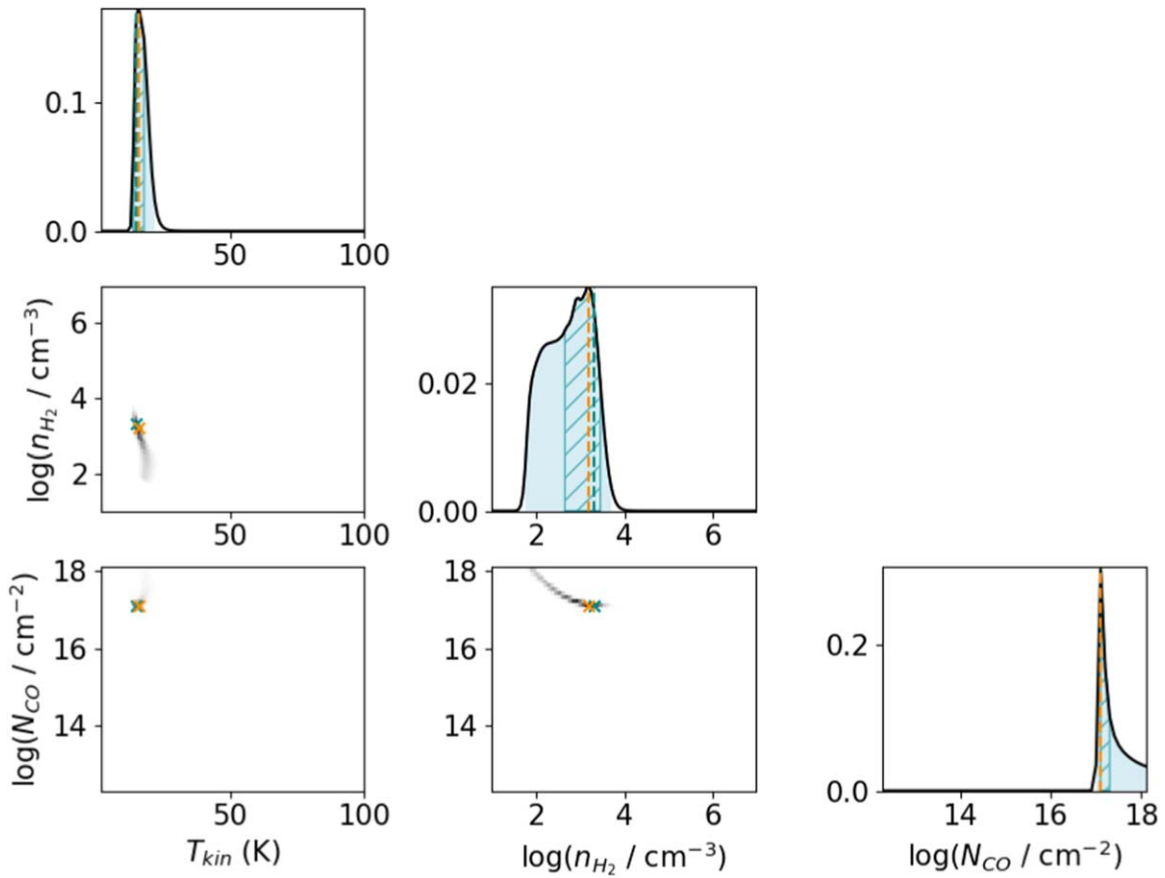


Figure 5. Example of a probability distribution from representative data with line intensities of 1.7 K, 0.2 K, 1.2 K, and 0.14 K for $^{12}\text{CO}(1-0)$, $^{13}\text{CO}(1-0)$, $^{12}\text{CO}(2-1)$, and $^{13}\text{CO}(2-1)$, respectively, using a 15% beam filling factor, and $R_{13} = 100$. The ranges on the axes show the full tested parameter space. The blue shading shows the 2.5 Bayesian intervals (“moderate” evidence), and the blue hatching shows the 1.0 Bayesian intervals (“weak” evidence). The vertical blue dashed lines and blue crosses indicate p_{max} , and the orange dashed lines and orange crosses indicate the maximum value of the probability profiles. This plot indicates that this pixel most likely has $T_{\text{kin}} = 15$ K, $n_{\text{H}_2} = 10^{3.3}$ cm^{-3} , and $N_{\text{CO}} = 10^{17.1}$ cm^{-2} .

these attempts, we used a range of filling factors from 10% to 20%. The lower limit of this range comes from unphysical fitting solutions (primarily defined as excessively large line-of-sight path lengths), and the upper limit comes from measured upper limits when comparing the high-resolution $^{13}\text{CO}(1-0)$ observations at $13''$ to the low-resolution maps at $45''$. The exception to this is the $\sim 2'$ region at 5:39:50–70:08:00, where we found a lower limit on the filling factor to be 15% rather than 10%. A filling factor of 10% results in line-of-sight path lengths that are > 100 pc, while the radius of the clouds in the region are measured to be ~ 20 pc. We do not take into account any potential difference in beam filling factors between different lines, despite them likely having different spatial distributions.

Using simulated data from the full range of the parameter space based on expected emission from RADEX and the measured rms error in the observed maps, we evaluated how well our data can be fit by the process described here. We also evaluated which of the Bayesian and confidence intervals best recovered true parameter values while still constraining their values. The full evaluation process is described in Appendix B, and additional related plots are available as supplementary material.¹² The true parameter values were almost always recovered at $N_{\text{CO}} > 10^{15} \text{ cm}^{-2}$ and for the full range of T_{kin} and n_{H_2} . The intervals that were determined to best characterize the true parameter values were a combination of the 95%

confidence interval and the 1.0 Bayesian interval. They showed similarly high recovery rates of the true parameter values and had the tightest constraints on those values. In some regions, the 95% confidence interval was better constrained than the 1.0 Bayesian interval, and vice versa, hence the combination of the two.

We also consider how the fitting process depends on including all four observed lines— $^{12}\text{CO}(1-0)$, $^{13}\text{CO}(1-0)$, $^{12}\text{CO}(2-1)$, and $^{13}\text{CO}(2-1)$ —and how it would change if we included only the three lines with the best angular resolution and dropped $^{12}\text{CO}(1-0)$, which has a resolution of $45''$. This would allow us to do the entire fitting process at higher resolution since we would instead be limited by the $^{13}\text{CO}(2-1)$ at $30''$. We consider this case in Appendix B.1 using the fitting evaluation methods described in Appendix B. We find that dropping the $^{12}\text{CO}(1-0)$ results in a loss of sensitivity to moderate values of N_{CO} . While the resulting fitted intervals still include the correct value almost all of the time for $N_{\text{CO}} > 10^{15} \text{ cm}^{-2}$, they are only well constrained for $N_{\text{CO}} > 10^{16} \text{ cm}^{-2}$. We decided that the improvement in resolution is not worth the loss in sensitivity to this range of column densities.

3.2. Generating Maps of Physical Parameters

We perform the RADEX fitting on each of the pixels in the map. For each velocity component within each pixel, we find the peak of the $^{13}\text{CO}(1-0)$ line profile for a single velocity

¹² <https://doi.org/10.5281/zenodo.4646288>

component and perform a full fit of the three physical parameters— T_{kin} , n_{H_2} , and N_{CO} —for the peak value. We then assume that T_{kin} and n_{H_2} are constant for that line of sight and fit the rest of the line only considering the T_{kin} and n_{H_2} that were in the fitted interval of the line peak to get N_{CO} across the line. We include only velocities for which at least two lines have detections above 5σ . N_{CO} is then summed over the line to get a total value for the pixel. Upper and lower errors come from the upper and lower bounds of the fitted interval for each parameter, and for N_{CO} , the upper errors and lower errors are propagated separately to get upper and lower errors on the total N_{CO} for the line.

We also considered two other methods for this fitting process: fitting all three parameters for each voxel along the line of sight or holding T_{kin} and n_{H_2} fixed for the entire cloud after segmenting the emission into clumps. These alternative methods are compared in Appendix C, where we find that the method described here of holding T_{kin} and n_{H_2} fixed for the line of sight yielded the most reliable realistic results.

This process was done once with $R_{13} = 50$ and once with $R_{13} = 100$, and also once each with a filling factor of 10% and 20% for a total of four runs, with the exception of the region around 5:39:50–70:08:00, for which we used a lower limit on the filling factor of 15% rather than 10%, as described in Appendix A. To correct our final results for this filling factor, we multiplied the fitted N_{CO} by the assumed filling factor for the clump. We did not correct the n_{H_2} values for the filling factor, so the values reported are those of clump structures on the scale of the assumed filling factor (4''5, 6''75 or 9'' for filling factor of 10%, 15%, or 20%, respectively).

When approaching a boundary between two velocity components, both spatially and in velocity space, we drew a hard barrier rather than doing any partial pixel assignments to account for overlapping line wings or spatial overlap. To check if this affected the fitting results, we did the RADEX fitting for three overlapping velocity components, but this time fitting Gaussian line profiles to each pixel to appropriately assign partial emission to the overlapping clumps. The RADEX-fitting code used this partial emission assignment and continued the fitting as before. This did not result in any significant change in any of the derived quantities, and so fortunately the detailed accounting of multiple velocity components does not need to be added in general to this kind of analysis. This is likely because the line wing that was cut from Component A and assigned to Component B is well accounted for by the line wing of Component B that was assigned to Component A, so the amount of emission is not significantly changed. This result might change if there is a large temperature difference between overlapping components, but that seems unlikely to occur in most scenarios.

The results for each velocity component were combined into maps of the whole Ridge shown in Figure 6 by adding N_{CO} along each line of sight and using a mass-weighted average for T_{kin} and n_{H_2} . We masked fits that were not well constrained since our results from Appendix B showed that poorly constrained fits often were also not accurate. How well each parameter could be expected to be constrained varied largely, as shown in Appendix B. T_{kin} and N_{CO} were both usually tightly constrained, while the fitted n_{H_2} is not as well constrained. This appears to be a reflection of how well the data at hand can inform the physical parameters rather than a reflection of how reliable the fitting process is. For both

Figure 6 and deriving quantities in Section 4.2, we masked values of N_{CO} where the error was more than 80%, T_{kin} where the error was more than 50%, and n_{H_2} where the error was more than 200%. We also masked values of T_{kin} that were less than 3 K, and values of n_{H_2} that rose sharply at the edges of clumps. In the case of the Molecular Ridge, we accomplished this by masking where n_{H_2} was greater than 10^4 cm^{-3} since values larger than that only occurred in edge pixels, but this would change if the range of fitted n_{H_2} had been higher.

After cutting pixels that had poorly constrained or unphysical fits, we combined fitted values from the runs with different R_{13} and filling factors. The reported values for T_{kin} , n_{H_2} , and N_{CO} are the mean of the best-fit values from the $R_{13} = 50$ and $R_{13} = 100$ results and the 10% and 20% filling factor results. The upper and lower errors are from the highest and lowest values included in any of the fitted intervals (i.e., if T_{kin} is 26 ± 3 K for $R_{13} = 50$ and 30 ± 5 K for $R_{13} = 100$, the reported T_{kin} is 28^{+7}_{-5} K). When reporting a single error, we use the geometric mean of the upper and lower error. This results in the maps shown in Figure 6 sometimes having larger errors than the cutoffs described here.

4. Clump Definitions and Properties

4.1. Clump Definitions

We used `quickclump`¹³(Sidorin 2017), which is a Python clump-finding algorithm that is similar in methodology to `clumpfind` (Williams et al. 1994) and `DENDROFIND` (Wünsch et al. 2012). These clumps are based on the ALMA $^{13}\text{CO}(1-0)$ cube convolved to 45'' to match the lowest-resolution observation (the $^{12}\text{CO}(1-0)$ from MAGMA), and the input parameters used were $N_{\text{levels}} = 1000$, $T_{\text{cutoff}} = 4\sigma = 1.4$ K, $d_{\text{leaf}} = 4\sigma = 1.4$ K, and $N_{\text{pixmin}} = 5$. A map of the 32 clumps identified by `quickclump` is shown in Figure 7 where they are also given identifying numbers. Each voxel in the data cube was assigned to at most a single clump, so overlapping clump borders in Figure 7 indicate that the clumps overlap along the line of sight and are differentiated by their velocity structure. The integrated line fluxes for each of these clumps and each observed line are given in Table 2. Clumps 3, 10, and 11 do not have corresponding APEX data and so were not included in the RADEX fitting.

If any clump had more than 75% of the pixels masked in any parameter, we removed the entire clump from the following analysis; this was only the case for n_{H_2} in clumps 1, 20, 29, 30, and 32. We also discarded the fits of clumps 9, 15, and 21 because they had very few pixels with successful fits, the fitted parameters had large variations from pixel to pixel, and they were major outliers in later trends.

4.2. Derived Clump Properties

For each clump, we calculated the mass by summing the N_{CO} within the clump, then multiplying by the area of each pixel in square centimeters, the ratio of H_2/CO , and a factor of 1.3 to convert from H_2 mass to total mass based on cosmic abundances. The H_2/CO ratio is based on the values of R_{13} for the map (either 50 or 100), and $\text{H}_2/^{13}\text{CO}$ in the outer Milky Way, where the metallicity is similar to the LMC ($\sim 1/3$ of solar). This has been measured to be between $\text{H}_2/^{13}\text{CO} = 10^6$ (Heyer et al. 2001) and $\text{H}_2/^{13}\text{CO} = 3 \times 10^6$

¹³ <https://github.com/vojtech-sidorin/quickclump/>

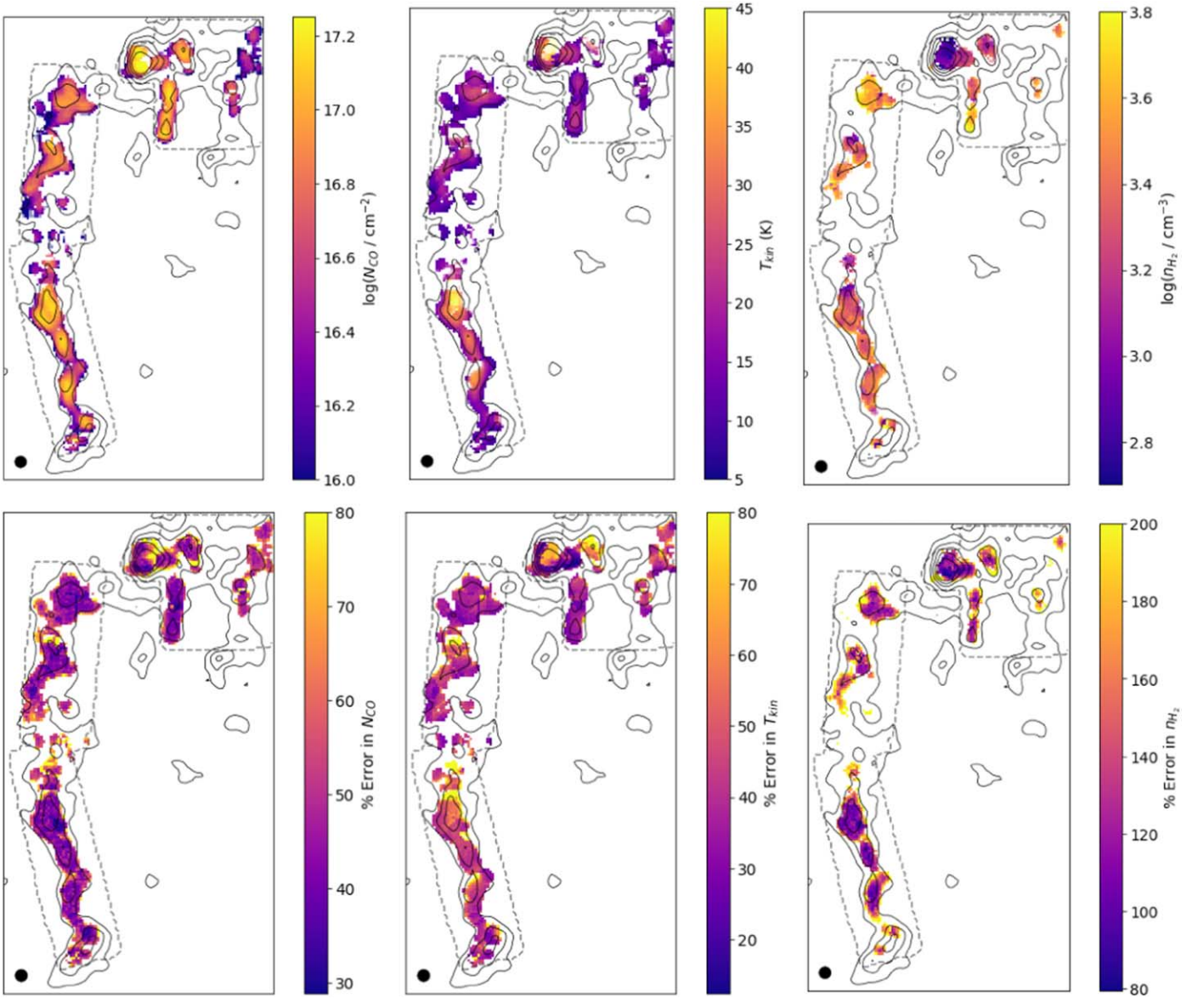


Figure 6. RADEX-fitted maps of N_{CO} , T_{kin} , and n_{H_2} (top row, left to right) and the percent error in N_{CO} , T_{kin} , and n_{H_2} (bottom row, left to right). N_{CO} was masked where the error was more than 80%, T_{kin} where the error was more than 50%, and n_{H_2} where the error was more than 200%. The values shown have been averaged between the values fit with $R_{13} = 50$ and $R_{13} = 100$ and filling factors of 10% and 20%, which can result in errors larger than the described cutoffs. The pixel transparency in the maps of the fitted parameters (top row) is proportional to the error in those parameters (bottom row). All N_{CO} values are corrected for the assumed beam filling factor, but the n_{H_2} values are those fitted to the structures at the filling factor scale ($4''/5$ or $9''$ for filling factors of 10% and 20%, respectively). The solid contours are the integrated intensity of MAGMA $^{12}\text{CO}(1-0)$, as shown in Figure 2, and the dashed contours show the common observational footprint. The $45''$ beam is shown in the bottom left corner.

(Brand & Wouterloot 1995), so we adopt $\text{H}_2/^{13}\text{CO} = 2 \times 10^6$ in this work. Previous works in the LMC have used similar values: $2\text{--}6 \times 10^6$ in Heikkilä et al. (1999), and 3×10^6 in Wong et al. (2019). We keep $\text{H}_2/^{13}\text{CO}$ constant rather than H_2/CO since ^{13}CO is optically thinner; ^{12}CO is usually optically thick, so the column density is more correlated with the ^{13}CO lines. Keeping $\text{H}_2/^{13}\text{CO}$ constant minimizes our dependence on the value assumed for R_{13} and instead leaves us with the value of $\text{H}_2/^{13}\text{CO}$ as the major systematic uncertainty.

The final mass estimate for the clump is the mean of the masses from assuming $R_{13} = 50$ and $R_{13} = 100$ and assuming a filling factor of 10% and 20%. The upper and lower errors come from the full range included in the upper and lower errors on the two masses, as described in Section 3.2. When a single

error is reported, it is the geometric mean of the upper and lower errors. To get temperatures and densities for each clump, we took the mass-weighted average of all pixels in the clump, with the upper and lower errors propagated through separately. The resulting clump masses are in the range $(3.4\text{--}35.5) \times 10^3 M_{\odot}$, temperatures are in the range 13–36 K, and densities are in the range $650\text{--}3940 \text{ cm}^{-3}$.

To measure the linewidths, we found the mass-weighted mean line profile using the map of N_{CO} . We then fit a Gaussian to this average line profile and report σ_v , not FWHM. The resulting linewidths are in the range $1.2\text{--}2.1 \text{ km s}^{-1}$. Shuffling the line profiles to a common central velocity first would change the linewidths by $\sim 10\%$.

To get the radius of the clumps, we fit ellipses to the half-light contour, giving us major and minor axes for the clump.

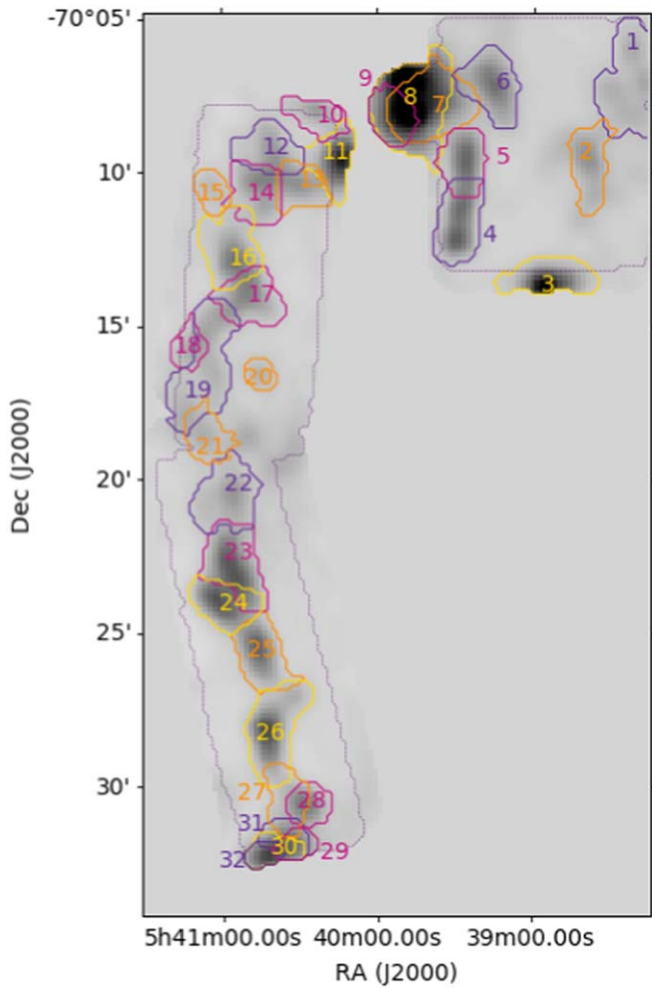


Figure 7. Projection of the 32 clumps identified by `quickclump` with identifying numbers. The grayscale is the integrated intensity of $^{13}\text{CO}(1-0)$ (same map as Figure 3). Overlapping clump borders indicate that the clumps overlap along the line of sight and are differentiated by their velocity structure. The dotted contour shows the common observational footprint of the four observed emission lines.

We convert these FWHM values to σ of a Gaussian profile ($\text{FWHM} = 2.35 \times \sigma$). The reported radius is the geometric mean of the major and minor axes.

We also compare the radii from the fitted ellipse to two other methods. One is finding the area of the clump within the half-light contour and then finding the radius of a circle with equivalent area. This is taken to be an effective FWHM, which is then converted to σ of a Gaussian profile. This results in an effective radius that is usually almost identical to the geometric mean of the fitted ellipse, differing by a factor of 0.99 on average.

The other method is to take the spatial second moment of the clump projected along the axes of the fitted ellipse. This results in σ for the major and minor axes of the clump. The geometric mean of these major and minor radii is a factor of 0.72 lower on average than that fitted by the ellipse.

In the rest of this paper, we use the radius from the ellipse fitting method, and the error in the radius takes into account how noncircular the clump boundary is. The resulting σ_r are in the range 5–10 pc.

The values of all derived properties for each of the clumps with RADEX fits are given in Table 3.

5. Associated YSOs

Current star formation in a molecular clump is expected to affect the gas in that clump—heating and changes in optical depth due to bulk gas motions and photodissociation will change the excitation conditions. In this section we describe the YSOs in the region, and how they are associated with CO clumps. In the next section, we will compare our non-LTE fitting to other techniques of determining gas properties, and will find that the presence of YSOs does not appear to affect one’s ability to calculate gas properties using those different methods. In Section 7, we will address the different question of whether the presence of the YSOs is correlated with changes in the physical properties.

5.1. YSO Selection

Complete infrared surveys of the LMC with Spitzer (SAGE; Meixner et al. 2006) and Herschel (HERschel Inventory of The Agents of Galaxy Evolution (HERITAGE); Meixner et al. 2013) enabled the uniform selection of massive young stellar objects (MYSOs) across the entire galaxy. Whitney et al. (2008, henceforth W08) used PSF-fit photometry from the SAGE legacy catalog and color selections between 1 and $10\ \mu\text{m}$, chosen to include MYSO models and exclude evolved and main-sequence stars. Gruendl & Chu (2009, henceforth GC09) used aperture photometry of SAGE images and the $4.5\text{--}8.0\ \mu\text{m}$ color plus manual examination of images and source environment. Seale et al. (2014, henceforth S14) used $250\ \mu\text{m}$ PSF-fit photometry from the HERITAGE legacy catalog and $24\ \mu\text{m}$ emission to include MYSOs and resolved morphology to exclude background galaxies.

We combined the three existing MYSO catalogs in the Ridge region, first by matching all GC09 and W08 sources within $10''$ of each S14 source. This resulted in the same associations that S14 published with a $5''$ matching radius, with the addition of a single matched source J85.202523–70.17060. Visual examination of $8.0\text{--}24\text{--}250\ \mu\text{m}$ three-color images prompted the removal of three S14 sources, which were blended with other S14 sources—the guiding principle being to identify the sources that could be reliably photometered over a wide wavelength range.

The resulting list of 109 sources contains 24 MYSO candidates identified only from the shorter-wavelength lists GC09 and W08, 45 identified only from the longer-wavelength list S14, and 40 sources identified in multiple lists and matched. Next, we generated cutout images from 1.0 to $500\ \mu\text{m}$ and calculated aperture photometry at all bands.

The data sets used are Two Micron All Sky Survey J , H , and K_s ($1.2\ \mu\text{m}$, $1.6\ \mu\text{m}$, and $2.1\ \mu\text{m}$, angular resolution $\sim 2''$, aperture radius $3''$; Skrutskie et al. 2006), SAGE Infrared Array Camera bands 1–4 (3.6 , 4.5 , 5.8 , and $8.0\ \mu\text{m}$, resolution $\sim 2''$, aperture radius $3''$) and Multiband Imaging Photometer for Spitzer (MIPS) $24\ \mu\text{m}$ and $70\ \mu\text{m}$ (resolution $6''$, $18''$, aperture radius $9''$, $18''$), HERITAGE PACS 110 and $170\ \mu\text{m}$ (resolution $8''$, $13''$, aperture radius $11''$, $18''$), and HERITAGE Spectral and Photometric Imaging REceiver 250 , 350 , $500\ \mu\text{m}$ (resolution $18''$, $25''$, $36''$, aperture radius $18''$, $25''$, $37''$). A local annular background was subtracted from each flux, and the uncertainty of the flux measurement is calculated from the standard deviation of values in the annulus.

We combined the published photometry with the new aperture photometry by visually inspecting the cutout images and spectral energy distribution (SED) of the two. For most sources, the published photometry agreed with the new

Table 2
Integrated Line Fluxes of Clumps

Clump	$^{12}\text{CO}(1-0)$	$^{12}\text{CO}(2-1)$	$^{13}\text{CO}(1-0)$	$^{13}\text{CO}(2-1)$	CS(2-1)
1	70.9 ± 0.4	62.7	5.4 ± 0.04	6.45	0.411 ± 0.04
2	46.3 ± 0.3	42.7	4.84 ± 0.04	4.18	0.229 ± 0.03
3	42.4 ± 0.3	—	6.97 ± 0.05	—	1.15 ± 0.03
4	75.7 ± 0.4	81.7	10.1 ± 0.06	14.4	3.07 ± 0.04
5	58.1 ± 0.3	57.9	8.67 ± 0.05	7.8	1.83 ± 0.03
6	100 ± 0.4	83.1	9.57 ± 0.05	8.1	0.699 ± 0.04
7	119 ± 0.5	98.1	10.5 ± 0.06	8.78	1.12 ± 0.04
8	277 ± 0.8	202	20.1 ± 0.08	14.6	2.68 ± 0.06
9	31.6 ± 0.3	28.4	2.47 ± 0.03	2.13	0.371 ± 0.03
10	12.4 ± 0.2	—	1.4 ± 0.02	—	0.27 ± 0.02
11	57.9 ± 0.3	—	6.2 ± 0.05	—	1.38 ± 0.03
12	44.6 ± 0.3	42.4	5.32 ± 0.04	5.19	0.463 ± 0.03
13	34.7 ± 0.3	38.6	4.96 ± 0.04	4.74	0.462 ± 0.03
14	53.5 ± 0.3	65.6	7.34 ± 0.05	9.21	0.816 ± 0.03
15	9.17 ± 0.1	11.2	0.988 ± 0.02	1.42	0.154 ± 0.02
16	75.9 ± 0.4	65.3	7.62 ± 0.05	6.33	0.335 ± 0.03
17	59.2 ± 0.3	55.4	7.29 ± 0.05	7.07	0.325 ± 0.03
18	14.6 ± 0.2	13.1	1.82 ± 0.02	1.98	0.0939 ± 0.02
19	77.6 ± 0.4	72.8	8.09 ± 0.05	7.89	0.416 ± 0.04
20	8.75 ± 0.1	9.12	1.03 ± 0.02	0.788	0.0461 ± 0.01
21	16.1 ± 0.2	12.5	1.54 ± 0.02	1.74	0.0953 ± 0.02
22	78.8 ± 0.4	65.7	6.37 ± 0.04	5.23	0.317 ± 0.03
23	151 ± 0.6	130	15.1 ± 0.07	15	1.34 ± 0.04
24	96.2 ± 0.5	99.1	11.2 ± 0.06	12.4	1.26 ± 0.03
25	79.6 ± 0.4	72.2	9.61 ± 0.06	9.74	0.898 ± 0.03
26	100 ± 0.5	93.6	13.3 ± 0.07	13.5	1.47 ± 0.04
27	26.6 ± 0.2	26.4	2.43 ± 0.03	2.83	0.269 ± 0.02
28	33.9 ± 0.3	31.6	3.8 ± 0.03	3.58	0.534 ± 0.02
29	9.18 ± 0.1	9.45	0.907 ± 0.02	1.17	0.321 ± 0.02
30	29.8 ± 0.2	30.7	2.29 ± 0.03	2.38	0.646 ± 0.03
31	16.8 ± 0.2	18.4	2.09 ± 0.03	1.8	0.24 ± 0.02
32	5.83 ± 0.1	4.79	0.403 ± 0.02	0.341	0.21 ± 0.01

Note. All line fluxes are integrated over the whole clump in units of $10^3 \text{ K km s}^{-1} \text{ arcsec}^2$. Clumps 3, 10, and 11 do not have corresponding APEX data. The uncertainty is a 10% error from the absolute flux calibration plus the rms error added in quadrature.

aperture photometry within uncertainties, so the average was used. For sources and bands in which the published photometry was lacking, the aperture photometry smoothly filled in the SED.

The Spitzer MIPS $70 \mu\text{m}$ resolution of $18''$ is significantly worse than the neighboring points in our SED (Spitzer MIPS $24 \mu\text{m}$ and Herschel PACS $100 \mu\text{m}$ at $\sim 6''$). Consequently, the $70 \mu\text{m}$ flux density was clearly affected by blending for many sources, so was used as an upper limit in the subsequent SED fitting. If the image cutouts were confused, or the aperture and published photometry were very discrepant for a given source and band, we either eliminated that band from the fitting or used the largest photometric value as an upper limit.

5.2. YSO Fitting

We fit the YSO SEDs with the Robitaille (2017) grid of single-YSO dust radiative transfer models¹⁴ and the Robitaille et al. (2007) χ^2 fitting code.¹⁵ Following many other studies (e.g., Carlson et al. 2012; Chen et al. 2010), we used a minimum uncertainty in each band of 10%, and calculated χ^2 for every model. Central sources in the Robitaille (2017) model grid are parameterized by the radius and temperature of the

YSO, R_* , and T_* . We interpolated the $Z = 0.004$ PAdova and TRieste Stellar Evolution Code stellar evolutionary models (Bressan et al. 2012) that include the pre-main-sequence phase¹⁶ to determine the mass of the YSO, M_* , and age for each Robitaille YSO model. The Robitaille circumstellar dust distribution is that of a rotating flattened toroid in analytical form (Ulrich 1976) parameterized by centrifugal radius R_C and scaling density ρ_0 . Using the central source mass assigned to each model, the envelope accretion rate \dot{M} is a function of M_* , ρ_0 , and R_C (Robitaille 2017, Equation (5)). The envelope accretion rate relative to the central source mass is a measure of evolutionary stage under the assumption that mean accretion rate decreases with time for protostars.

Finally, we assigned M_* and \dot{M} to each source in the Ridge by marginalizing the model probability distributions over all other model parameters and measuring the first and second moments of each one-dimensional probability distribution. We visually inspected the two-dimensional probability distribution of M_* and \dot{M} for each source and verified that the second moments that we are using as uncertainties for those parameters do indeed span the range of well-fitting models, even in the minority of cases where the probability distribution is not single-peaked. A table of M_* and \dot{M} for each YSO that was matched with a CO clump is given in Table 4.

¹⁴ <https://zenodo.org/record/166732>

¹⁵ <https://sedfitter.readthedocs.io/en/stable/index.html>

¹⁶ <http://stev.oapd.inaf.it/cgi-bin/cmd>

Table 3
Derived Clump Properties

Clump ^a	Mass ^{b,c} ($10^3 M_\odot$)	n_{H_2} ^{b,c} (10^3 cm^{-3})	T_{kin} ^{b,c} (K)	σ_v ^c (km/s)	σ_R ^c (pc)	α_{vir} ^d	Number of YSOs ^e	Total M YSOs ^e (M_\odot)
2	$9.5^{+2.5}_{-0.62}$	$2.1^{+2}_{-0.75}$	17^{+15}_{-6}	2.3 ± 0.034	6.6 ± 3.7	7.9 ± 4.6	2	8.5 ± 1.2
4	$22^{+0.63}_{-0.54}$	$3.7^{+2.2}_{-0.81}$	$18^{+5.6}_{-5.1}$	1.8 ± 0.017	8 ± 4.5	2.7 ± 1.5	3	47 ± 4.9
5	$19^{+0.83}_{-0.61}$	$2^{+1.2}_{-0.53}$	$16^{+5.1}_{-4.5}$	1.9 ± 0.024	7 ± 2.6	3.1 ± 1.2	0	...
6	$19^{+1.8}_{-0.39}$	$1.6^{+0.94}_{-0.59}$	$23^{+13}_{-8.6}$	1.8 ± 0.014	7.4 ± 2.4	3 ± 0.98	0	...
7	$18^{+0.95}_{-0.5}$	$1.7^{+0.59}_{-0.26}$	$19^{+4.9}_{-3.3}$	1.5 ± 0.0076	8.9 ± 3.8	2.6 ± 1.1	1	6.5 ± 0.87
8	$36^{+4.5}_{-2.1}$	$0.65^{+0.46}_{-0.35}$	32^{+21}_{-10}	2.2 ± 0.0096	9.3 ± 2.2	2.7 ± 0.68	0	...
12	$10^{+0.42}_{-0.34}$	$3.8^{+2.6}_{-1.3}$	$18^{+5.6}_{-5.2}$	0.97 ± 0.0057	6.7 ± 0.6	1.4 ± 0.13	2	13 ± 1.5
13	$10^{+1.2}_{-0.83}$	$2.4^{+1.8}_{-0.88}$	$20^{+8.8}_{-6.9}$	1.2 ± 0.007	7.3 ± 1.3	2.2 ± 0.47	0	...
14	$15^{+0.35}_{-0.25}$	$3.9^{+2.2}_{-1.1}$	$20^{+6.6}_{-6}$	1.6 ± 0.012	7.8 ± 0.96	3 ± 0.37	5	52 ± 3.8
16	$16^{+2.1}_{-1.3}$	$1.3^{+0.77}_{-0.44}$	$23^{+18}_{-9.9}$	2 ± 0.035	6.7 ± 0.91	3.7 ± 0.66	0	...
17	$15^{+0.43}_{-0.23}$	$2.5^{+1.1}_{-0.52}$	$19^{+7.3}_{-5.9}$	1.3 ± 0.0087	8 ± 0.48	1.9 ± 0.12	2	5.9 ± 0.83
18	$3.6^{+0.22}_{-0.16}$	$3.2^{+3.6}_{-0.94}$	13^{+4}_{-5}	1.1 ± 0.029	4.8 ± 0.84	3.5 ± 0.66	1	12 ± 1.5
19	$14^{+0.73}_{-0.58}$	$2.7^{+2}_{-0.95}$	$17^{+5.6}_{-5}$	1.8 ± 0.025	10 ± 5	5.3 ± 2.6	0	...
22	$11^{+1.1}_{-0.4}$	$1.2^{+1.4}_{-0.79}$	$23^{+9}_{-9.2}$	1.8 ± 0.013	7.9 ± 1.6	5.1 ± 1.1	0	...
23	$30^{+2.1}_{-2.4}$	$1.7^{+0.88}_{-0.53}$	36^{+22}_{-16}	1.7 ± 0.0078	8.5 ± 2.5	1.7 ± 0.53	0	...
24	$22^{+1.2}_{-1.1}$	$2.6^{+1.2}_{-0.8}$	29^{+13}_{-10}	1.6 ± 0.0088	7.7 ± 1.5	2.1 ± 0.43	2	29 ± 3.1
25	$19^{+0.95}_{-0.89}$	$2.4^{+1}_{-0.63}$	$25^{+10}_{-8.2}$	1.2 ± 0.01	7.2 ± 2.5	1.2 ± 0.42	1	5 ± 1.7
26	$26^{+1.4}_{-0.89}$	$2.5^{+1.2}_{-0.8}$	$24^{+11}_{-8.2}$	1.4 ± 0.011	6.9 ± 2.2	1.2 ± 0.39	5	45 ± 4
27	$4.1^{+0.28}_{-0.22}$	$1.8^{+2}_{-0.68}$	$17^{+6.1}_{-5}$	0.97 ± 0.012	6.1 ± 1.1	3.1 ± 0.59	1	4.9 ± 0.65
28	$8.1^{+2.3}_{-1.2}$	$3^{+3.9}_{-1.2}$	21^{+23}_{-11}	2.1 ± 0.037	5.1 ± 0.28	6.2 ± 1.3	1	3.2 ± 1.1
31	$3.4^{+0.28}_{-0.21}$	$2.6^{+2.1}_{-0.75}$	$16^{+5.9}_{-4.8}$	1.1 ± 0.02	4.9 ± 0.43	3.7 ± 0.43	0	...

Notes.

^a CO clump identifying numbers are shown in Figure 7. Clumps 3, 10, and 11 are not included because they do not have corresponding APEX data. Clumps 1, 20, 29, 30, and 32 are not included because more than 75% of the pixels had poor RADEX fits for n_{H_2} . Clumps 9, 15, and 21 are not included because the RADEX fits had unphysical variations between pixels.

^b Result of RADEX fitting.

^c Calculation described in Section 4.2.

^d Calculated with Equation (7).

^e Identifying YSOs, matching them to associated CO clumps, and fitting YSO masses is described in Section 5.

It is important to recognize that despite the use of a specific set of models, fundamentally the quantities being measured and parameterized are the total luminosity of the central source, which is tightly correlated with the derived M_\star , and the amount of dust extinction around that central source, which is highly correlated with the envelope accretion rate \dot{M} (except for more evolved sources that have little envelope, in which case the disk has more of an effect on the SED).

Comparing the detection limits of the SAGE and Herschel surveys to all of the Robitaille (2017) models, we expect that all protostars with a mass above $6 M_\odot$ will be detected. At $2.5 M_\odot$, half of all protostars would be detected, though it is possible to detect some protostars down to $1 M_\odot$, depending on their evolutionary state.

5.3. YSO Matching

We then matched the YSOs to CO clumps by eye, assigning them to a clump only if their positions coincided with CO emission (see Figure 8). In cases where the YSO overlapped with strong emission from more than one clump, it was assigned to the clump that was brightest in its location. This process resulted in 37 of the YSOs being matched to CO clumps in the Molecular Ridge. Of these 37, nine were associated with the three clumps that do not have data for $^{12}\text{CO}(2-1)$ and $^{13}\text{CO}(2-1)$ from APEX (clumps 3, 10, and 11) and so could not be included in all parts of the analysis. Table 4

includes the number of the clump assigned to each of these 37 YSOs.

6. Comparing RADEX Fitting to Other Methods

6.1. LTE Method

We compared the clump masses derived by the RADEX fitting to the results of LTE assumptions with both the (1-0) lines and the (2-1) lines. For LTE, we use the peak of the ^{12}CO line for each pixel, divided by a beam filling factor of 10% or 20% that we used in the RADEX fitting (results for each were later combined, as described in Section 3.1), to get T_{ex} :

$$T_B = T_{ul}(1 - e^{-\tau_\nu}) \left[\frac{1}{e^{T_{ul}/T_{\text{ex}}} - 1} - \frac{1}{e^{T_{ul}/T_{\text{bg}}} - 1} \right], \quad (4)$$

where we assume optically thick ^{12}CO , so $e^{-\tau_\nu} \approx 0$. T_B is the peak brightness temperature for the pixel divided by the filling factor, $T_{ul} = 5.532$ K for $^{12}\text{CO}(1-0)$, $T_{ul} = 11.06$ K for $^{12}\text{CO}(2-1)$, and $T_{\text{bg}} = 2.73$ K. Then, we calculate the optical depth of ^{13}CO from

$$\tau_\nu = -\ln \left[1 - \frac{T_B}{T_{ul}} \left[\frac{1}{e^{T_{ul}/T_{\text{ex}}} - 1} - \frac{1}{e^{T_{ul}/T_{\text{bg}}} - 1} \right]^{-1} \right] \quad (5)$$

where now T_B is from $^{13}\text{CO}(1-0)$ divided by the filling factor of 10%, $T_{ul} = 5.289$ K for $^{13}\text{CO}(1-0)$, and $T_{ul} = 10.58$ K for

Table 4
Fitted YSO Properties

Name	M_* (M_\odot)	$\log(\dot{M})$ ($M_\odot \text{ yr}^{-1}$)	Clump Assignment
J84.636381-70.144787	4.9 ± 0.8	-5.2 ± 0.3	1
J84.677275-70.194884	4.8 ± 1.0	-5.2 ± 0.3	2
J84.663696-70.163174	3.7 ± 0.5	-5.2 ± 0.3	2
J84.722292-70.227647	4.9 ± 0.6	-4.6 ± 0.3	3
J84.739529-70.22909	15.4 ± 2.0	-6.8 ± 0.3	3
J84.815252-70.224064	9.2 ± 2.4	-8.0 ± 1.1	3
J84.746459-70.227471	8.6 ± 1.2	-4.6 ± 0.3	3
J84.829777-70.220668	11.5 ± 1.6	-11.3 ± 0.4	3
J84.879808-70.20452	21.8 ± 3.9	-7.4 ± 0.3	4
J84.879594-70.200559	20.5 ± 2.7	-9.1 ± 0.3	4
053925.03-701255.0	4.6 ± 1.3	-6.1 ± 0.5	4
J84.962153-70.133828	6.5 ± 0.9	-4.6 ± 0.3	7
J85.101423-70.133438	11.2 ± 1.8	-8.6 ± 0.4	10
J85.057077-70.165809	15.1 ± 2.7	-10.1 ± 0.7	11
J85.050246-70.168067	15.4 ± 2.0	-11.6 ± 0.7	11
054012.00-700916.0	15.3 ± 2.1	-6.3 ± 0.3	11
054037.80-700914.0	6.5 ± 0.9	-8.7 ± 0.5	12
J85.18818-70.154154	6.2 ± 1.2	-8.0 ± 0.8	12
J054036.65-701201.1	4.2 ± 1.3	-8.1 ± 1.4	14
J85.179372-70.186003	15.4 ± 2.0	-7.9 ± 0.3	14
J85.193443-70.189071	15.4 ± 2.1	-6.8 ± 0.3	14
J85.207422-70.169937	8.1 ± 1.5	-4.6 ± 0.3	14
J85.192755-70.17054	8.5 ± 1.3	-4.6 ± 0.3	14
J85.225346-70.235587	4.7 ± 0.8	-5.2 ± 0.3	17
054054.33-701318.8	1.2 ± 0.1	-7.8 ± 0.5	17
J85.317317-70.265032	11.5 ± 1.5	-9.1 ± 0.3	18
J85.276729-70.393765	20.5 ± 2.7	-9.1 ± 0.3	24
054113.61-702329.1	9.0 ± 1.5	-7.8 ± 0.5	24
J054047.85-702551.1	5.0 ± 1.7	-8.0 ± 1.5	25
J85.18708-70.468313	20.5 ± 2.7	-6.8 ± 0.3	26
J85.180541-70.480586	6.5 ± 0.9	-4.6 ± 0.3	26
054044.25-702824.7	6.9 ± 2.0	-5.8 ± 0.4	26
054043.94-702918.5	4.6 ± 1.7	-7.9 ± 1.6	26
054038.61-702800.5	6.6 ± 1.0	-6.9 ± 0.3	26
J85.143381-70.523952	4.9 ± 0.6	-5.2 ± 0.3	27
J85.133273-70.508695	3.2 ± 1.1	-5.2 ± 0.3	28
J054026.85-703202.9	2.1 ± 0.3	-11.3 ± 0.3	29

$^{13}\text{CO}(2-1)$. Then, the column density of ^{13}CO is

$$N_{13} = \frac{8\pi\nu_0^2 Q}{c^2 A_{ul} g_u} \frac{1}{1 - e^{-T_{ul}/T_{\text{ex}}}} \int \tau_\nu d\nu \quad (6)$$

where we use $Q = \frac{T_{\text{ex}}}{B_0} + \frac{1}{3}$ and $B_0 = 2.644$ K for ^{13}CO . We adopt $\text{H}_2/^{13}\text{CO} = 2 \times 10^6$ and sum over all pixels in the clump to get masses from the LTE assumptions. A comparison of the results using the (1-0) and (2-1) lines against our RADEX-fitting method is given in Table 5.

Using (2-1) lines with the LTE assumptions results in a much lower mass estimate and a lower T_{ex} estimate than the RADEX-fitted T_{kin} (by average factors of 0.55 ± 0.10 and 0.78 ± 0.15 , respectively). A low mass estimate from LTE calculations is expected if ^{13}CO is sub-thermally excited and $T_{\text{ex}}^{13} < T_{\text{ex}}^{12}$. The T_{ex} derived from ^{12}CO is too high for ^{13}CO , which makes the optical depth of ^{13}CO underestimated, and so the column density and mass are underestimated (e.g., Castets et al. 1990; Padoan et al. 2000; Heyer & Dame 2015). The temperature estimate being lower than the non-LTE T_{kin} could mean that ^{12}CO is also sub-thermally excited, but less so than ^{13}CO .



Figure 8. The 28 YSOs that were matched to CO clumps with RADEX fits are shown as white circles, the nine YSOs that were matched to CO clumps that could not be fitted are shown as cyan squares, and the YSOs with no associated clump in $^{13}\text{CO}(1-0)$ are shown as red “X”s. The color image is the integrated intensity of $^{13}\text{CO}(1-0)$ (same maps as Figure 3), which is the map that was used to assign clumps with quickclump. The contours are the integrated intensity of $^{12}\text{CO}(1-0)$ as in Figure 2.

Table 5
Comparison of Methods

	M/M_{RF}	$T_{\text{ex}}/T_{\text{kin,RF}}$
LTE (1-0)	1.66 ± 0.19	0.71 ± 0.10
LTE (2-1)	0.55 ± 0.10	0.78 ± 0.15
X_{CO}	1.20 ± 0.33	NA

Note. Comparison of different methods of determining mass (from N_{CO}) and T_{kin} or T_{ex} . These values are the average of the ratios for all of the clumps that were fit with these methods and the standard deviation among the clumps. M_{RF} , $T_{\text{kin,RF}}$ are the values derived from the RADEX fitting as described in Section 3.2.

The mass estimate when using the (1-0) lines is higher than our fitted RADEX (by an average factor of 1.66 ± 0.19), which is harder to explain, though not unprecedented

(Indebetouw et al. 2020). One way this could happen is if the ^{12}CO is not actually optically thick, which would make the LTE T_{ex} estimate too low and shift the optical depth estimate higher. This could be exacerbated if the beam filling factor we use is too large, which would also artificially lower the measured excitation temperature. The nonlinearity of the LTE equations means that an underestimated T_{ex} due to a high filling factor would cause a larger shift to high column density than is corrected for, with the filling factor being multiplied back in at the end. This filling factor was also used in the RADEX fitting, but the nonlinearity of that is even more extreme, making it difficult to predict how much it would affect our results relative to the LTE calculations.

6.2. X_{CO} Method

We also include in Table 5 a comparison of the mass from a typical Milky Way value of $X_{\text{CO}} = 2 \times 10^{20} \text{ cm}^2/(\text{K km s}^{-1})$ (Bolatto et al. 2013). These masses are on average slightly higher than those fit with RADEX—though they are consistent within the deviation between clumps (the average factor is 1.20 ± 0.33).

We fit the linear relation between the RADEX-fitted total N_{H_2} and the summed $^{12}\text{CO}(1-0)$ flux of the clump in units of K km s^{-1} (W_{CO}), both divided by the number of pixels in the clump with N_{H_2} solutions (Figure 9(a)). The linear trend was fit to the linear values, not in log space. Values of individual pixels within the clumps with N_{H_2} solutions are also shown behind the clump average points. The slope of this trend is the X_{CO} conversion factor ($N_{\text{H}_2} = X_{\text{CO}} \times W_{\text{CO}}$). This relation is subject to the systematic error in the ratio $\text{H}_2/^{13}\text{CO}$ used in Section 4.2. We use $\text{H}_2/^{13}\text{CO} = 2 \times 10^6$ with a range of $(1 - 3) \times 10^6$ (Brand & Wouterloot 1995; Heikkilä et al. 1999; Heyer et al. 2001). A higher $\text{H}_2/^{13}\text{CO}$ value results in higher derived masses and a larger derived X_{CO} .

Fitting a linear relation results in a value for X_{CO} of $(1.81 \pm 0.1) \times 10^{20} \text{ cm}^2/(\text{K km s}^{-1})$, and taking into account the full systematic range due to the uncertainty in $\text{H}_2/^{13}\text{CO}$ and the error in the fitted X_{CO} results in a value of X_{CO} in the range $(0.85 - 2.87) \times 10^{20} \text{ cm}^2/(\text{K km s}^{-1})$, shown in Figure 9(a). This is lower than we expect for the Ridge since the LMC has a metallicity of one-third solar and has been estimated to have a value closer to $X_{\text{CO}} \sim 4 \times 10^{20} \text{ cm}^2/(\text{K km s}^{-1})$ (Hughes et al. 2010; Bolatto et al. 2013). This discrepancy could be because the non-LTE fitting is more accurate than previous measures or could be due to an underestimate of the $\text{H}_2/^{13}\text{CO}$ ratio; a ratio of $\text{H}_2/^{13}\text{CO} \sim 4 \times 10^6$ would make our fitted X_{CO} consistent with other estimates for the LMC.

We also perform this fitting with the summed $^{13}\text{CO}(1-0)$ intensities to get a value of $X_{13\text{CO}}$ (Figure 9(b)). We find a value of $X_{13\text{CO}} = (1.62 \pm 0.03) \times 10^{21} \text{ cm}^2/(\text{K km s}^{-1})$, and taking into account the systematic range of $\text{H}_2/^{13}\text{CO} = (1 - 3) \times 10^6$ and the error in the fitted $X_{13\text{CO}}$ results in a $X_{13\text{CO}}$ range of $(0.80 - 2.48) \times 10^{21} \text{ cm}^2/(\text{K km s}^{-1})$.

The relation between N_{H_2} and ^{13}CO emission is tighter than the relation of N_{H_2} with ^{12}CO . The fitted X_{CO} has a 5.8% error and a residual variance of 39, while the fitted $X_{13\text{CO}}$ has a 1.9% error and a residual variance of 4.3. Calculating a Pearson correlation coefficient for the two trends results in a value of $r = 0.62$ for X_{CO} and $r = 0.94$ for $X_{13\text{CO}}$. This shows that using an $X_{13\text{CO}}$ would be a more precise method of determining mass than X_{CO} , which makes sense since ^{13}CO is more optically thin

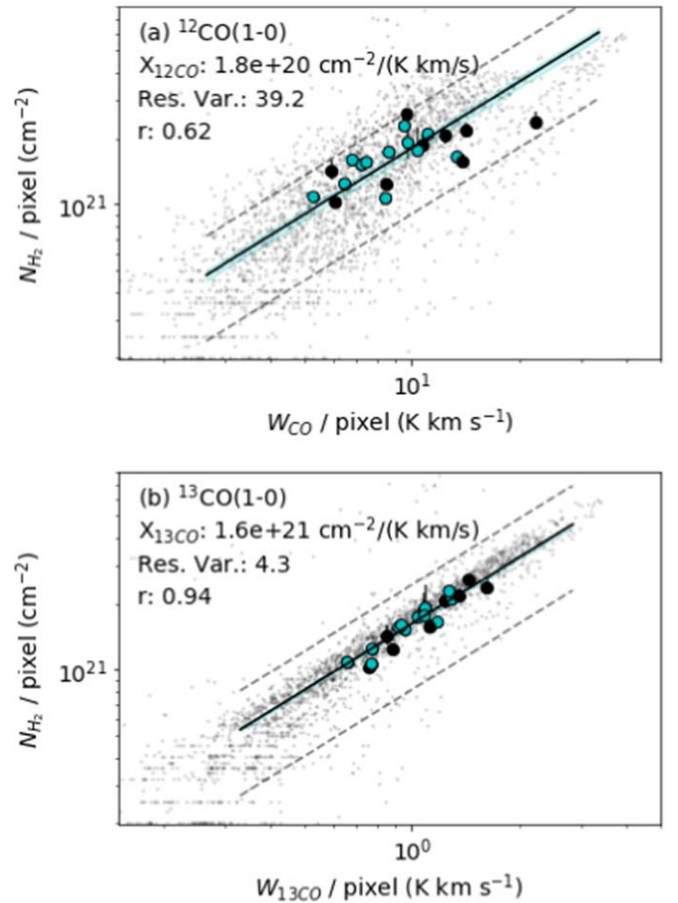


Figure 9. Fitted values of N_{H_2} per pixel against the integrated flux per pixel of $^{12}\text{CO}(1-0)$ (top) and $^{13}\text{CO}(1-0)$ (bottom). Blue circles indicate clumps with at least one associated YSO, while the black circles are clumps without any associated YSOs. The small black points show the values of individual pixels. The fitted linear trend (fitted linearly, not in log space as is plotted here) corresponds to a value of $X_{\text{CO}} = (1.8 \pm 0.1) \times 10^{20} \text{ cm}^2/(\text{K km s}^{-1})$ and $X_{13\text{CO}} = (1.6 \pm 0.03) \times 10^{21} \text{ cm}^2/(\text{K km s}^{-1})$, respectively. The dotted lines on either side show the systematic range from the uncertainty in the ratio $\text{H}_2/^{13}\text{CO}$ used to get N_{H_2} . ^{13}CO has a tighter trend with N_{H_2} with a residual variance of 4.3 and correlation coefficient of 0.94, while ^{12}CO has a residual variance of 39 and correlation coefficient of 0.62, suggesting that the $X_{13\text{CO}}$ factor may be a better tool for estimating mass than the typical X_{CO} .

and so can better trace the quantity of gas, while ^{12}CO is usually optically thick.

Another possible source of scatter for ^{12}CO could be the faint pixels that do not have corresponding ^{13}CO emission. Since detections in three of the four lines were required before the fitting proceeded, there are several pixels that have $^{12}\text{CO}(1-0)$ emission above 5σ but no emission in two of the other lines. These are the faintest of the pixels and so would have correspondingly low N_{CO} , so including them would not make large changes to the reported N_{H_2} or W_{CO} , but could account for some of the scatter.

We also show in both panels of Figure 9 the values of N_{H_2} and W_{CO} for individual pixels. In both cases, the pixels have shallower slopes than the clump-averaged values, and fitting the pixels instead would result in a value of $X_{\text{CO}} = (1.13 \pm 0.01) \times 10^{20} \text{ cm}^2/(\text{K km s}^{-1})$ and $X_{13\text{CO}} = (1.32 \pm 0.01) \times 10^{21} \text{ cm}^2/(\text{K km s}^{-1})$. For X_{CO} , the pixels show a stronger correlation between W_{CO} and N_{H_2} than the clump-averaged values, with a correlation coefficient of $r = 0.74$. In contrast, the clump-averaged values for $X_{13\text{CO}}$ have a stronger

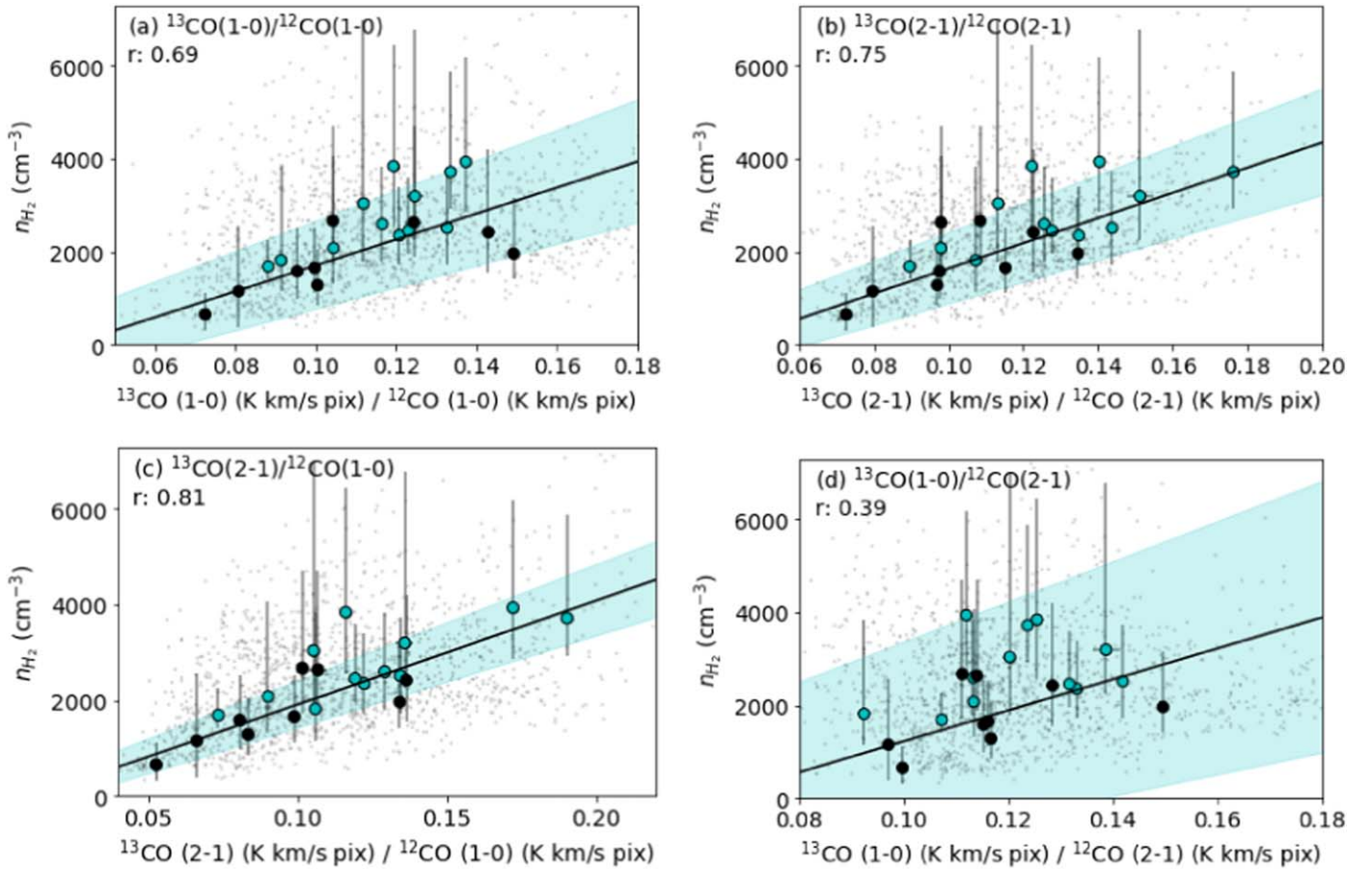


Figure 10. Volume density fitted by RADEX plotted against ratios of ^{13}CO to ^{12}CO . The ratio with the strongest correlation is $^{13}\text{CO}(2-1)/^{12}\text{CO}(1-0)$ in panel (c), with a residual variance of 0.18 and Pearson correlation coefficient of $r = 0.81$. The ratios $^{13}\text{CO}(1-0)/^{12}\text{CO}(1-0)$ and $^{13}\text{CO}(2-1)/^{12}\text{CO}(2-1)$ both also show strong trends with residual variances of 0.32 and 0.24, respectively, and $r = 0.69$ and $r = 0.75$, respectively. The ratio of $^{13}\text{CO}(1-0)/^{12}\text{CO}(2-1)$ shows very little trend with a residual variance of 0.57 and $r = 0.39$. Plot symbols are the same as in Figure 9. The blue points indicate clumps with at least one associated YSO, demonstrating that YSO presence does not appear to affect the trends at all.

trend than the pixels, which have a correlation coefficient of $r = 0.89$. We would expect the clump-averaged values to show a stronger trend since the X_{CO} method works best when integrating over variations in physical conditions (Bolatto et al. 2013).

6.3. Diagnostic Line Ratios

6.3.1. Isotopologues

Ratios of isotopologues (e.g., $^{13}\text{CO}/^{12}\text{CO}$) can trace volume density in the case where one line is optically thick and the other line is sub-thermally excited (Nishimura et al. 2015). We examine how well the ratios of the ^{13}CO and ^{12}CO lines' total fluxes in K km s^{-1} predict the fitted RADEX volume density, n_{H_2} . Figure 10 shows that the strongest combination of lines to predict n_{H_2} is $^{13}\text{CO}(2-1)/^{12}\text{CO}(1-0)$, with a residual variance of 0.18 and Pearson correlation coefficient of $r = 0.81$. This makes sense since we expect $^{13}\text{CO}(2-1)$ to be the most sub-thermally excited of the lines, especially from the LTE comparison in Section 6.1, and we expect $^{12}\text{CO}(1-0)$ to be the most optically thick.

The weakest predictor of n_{H_2} is $^{13}\text{CO}(1-0)/^{12}\text{CO}(2-1)$, with a residual variance of 0.57 and $r = 0.39$. $^{13}\text{CO}(1-0)/^{12}\text{CO}(1-0)$ and $^{13}\text{CO}(2-1)/^{12}\text{CO}(2-1)$ have residual variances of 0.32 and 0.24, respectively, and $r = 0.69$ and $r = 0.75$, respectively. All of these combinations do show a positive trend, indicating that

$^{13}\text{CO}/^{12}\text{CO}$ is indeed a good diagnostic of gas density in this physical regime, where the ^{13}CO is sub-thermally excited. In areas of higher temperature and density where all lines become thermalized, this relation would likely no longer hold.

The fitted n_{H_2} has asymmetrical error bars, and when fitting the trends in Figure 10, we simply use the mean of the upper and lower errors. This results in overestimated errors (Barlow 2004), but a proper treatment of the errors would require a computationally rigorous analysis to properly account for the non-Gaussian nature of the n_{H_2} probability distribution. We decided to report the simpler analysis with the acknowledgment that the errors are overestimated. Since the mean errors are usually lower than the upper errors and larger than the lower errors, the fit is also likely biased toward lower values of n_{H_2} .

In all plots, we indicate the clumps that have at least one associated YSO as blue instead of black. Although YSOs could potentially affect the excitation, we do not see any indication that the presence of YSOs affects our ability to recover and understand that excitation, using different methods.

We also show in Figure 10 the values for individual pixels. In all panels, the correlation of the pixels is much weaker than that of the clump-averaged values, having correlation coefficients of 0.35, 0.43, 0.53, and 0.11, respectively, for panels (a)–(d). This indicates that these trends are most accurate when averaged over the whole clump.

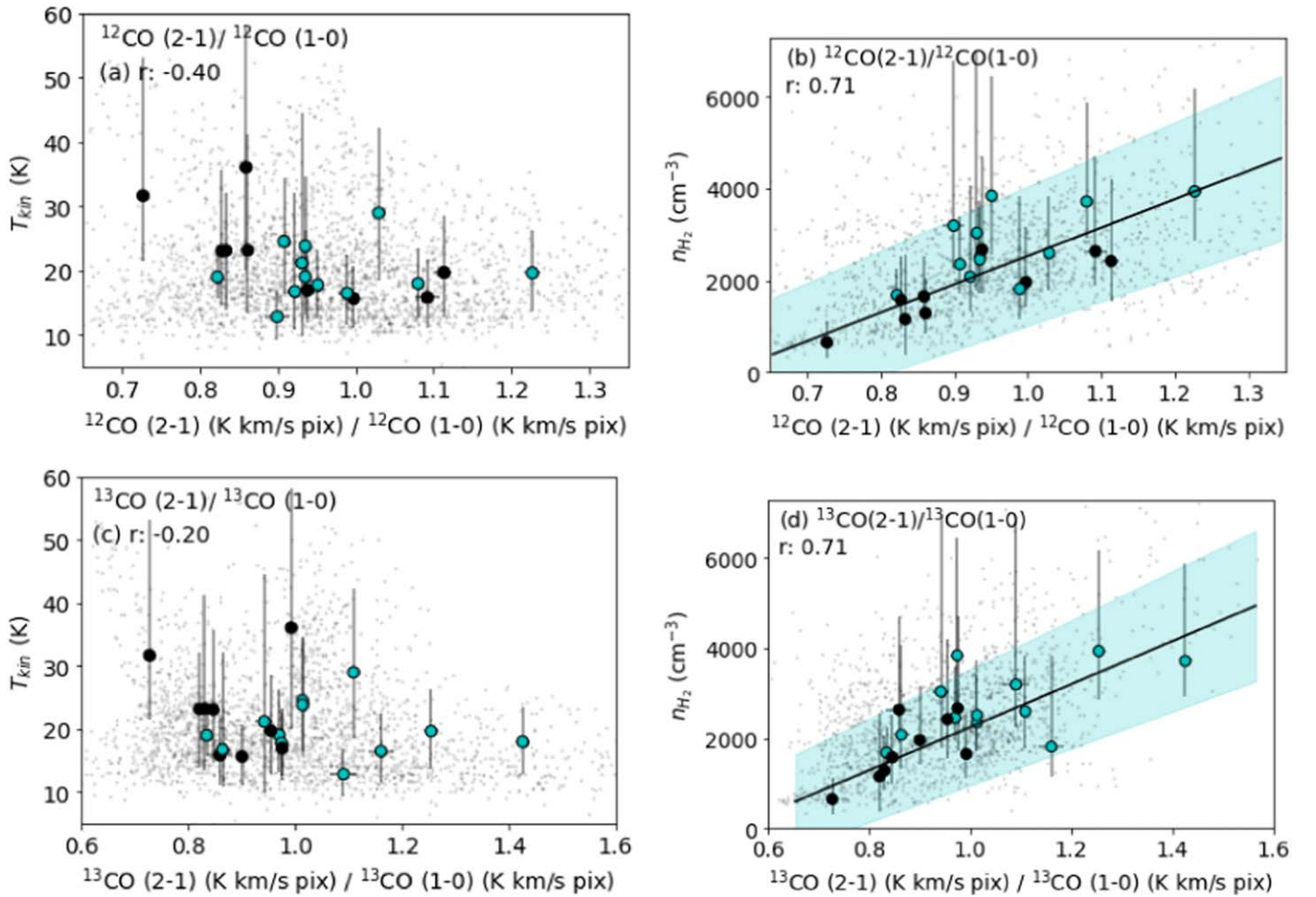


Figure 11. Kinetic temperature (left column) and RADEX-fitted density (right column) against ratios of upper and lower transitions ($^{12}\text{CO}(2-1)/^{12}\text{CO}(1-0)$ above and $^{13}\text{CO}(2-1)/^{13}\text{CO}(1-0)$ below). There is not a strong correlation with T_{kin} for either ^{12}CO or ^{13}CO , suggesting that such line ratios are not a good diagnostic of kinetic temperature in this physical regime. They do, however, show a correlation with density, which has been fitted with a linear trend. The two ratios have a similar correlation, both with $r = 0.71$ and residual variances of 0.22 and 0.25, respectively, though this is not as strong as the correlation of n_{H_2} with $^{13}\text{CO}(2-1)/^{12}\text{CO}(1-0)$ (Figure 10(c)). Plot symbols are the same as in Figure 9. Blue points indicate clumps with at least one associated YSO, which shows that YSO presence seems to have no effect on these trends, except that all clumps that have $^{13}\text{CO}(2-1)/^{13}\text{CO}(1-0) > 1$ also have at least one associated YSO.

6.3.2. Excitation Levels

Ratios of upper to lower excitation levels of CO (e.g., $^{12}\text{CO}(2-1)/^{12}\text{CO}(1-0)$) scale with excitation temperature and density when both lines are optically thin, and the ratio approaches unity as the lines get increasingly optically thick (Sakamoto 1994; Nishimura et al. 2015; Peñaloza et al. 2017). Figure 11 show the measured ratios of the total flux in K km s^{-1} pix for $^{12}\text{CO}(2-1)/^{12}\text{CO}(1-0)$ and for $^{13}\text{CO}(2-1)/^{13}\text{CO}(1-0)$ plotted against the RADEX-fitted T_{kin} and n_{H_2} .

The plots of T_{kin} against $^{12}\text{CO}(2-1)/^{12}\text{CO}(1-0)$ and $^{13}\text{CO}(2-1)/^{13}\text{CO}(1-0)$ in Figure 11 do not show a strong linear trend ($r = -0.40$ and $r = -0.20$, respectively). This could be because the line ratios do not correlate with the excitation temperature, or because the excitation temperature is not correlated with the kinetic temperature in these clumps. We have seen in Sections 6.1 and 6.3.1 that the lines are likely subthermally excited, which would be consistent with the excitation temperature not tracing the kinetic temperature as well.

The ratios of excitation levels seem much more correlated with n_{H_2} than T_{kin} . For these, we were able to fit a linear relation as shown in Figure 11. The two ratios have a similar

correlation, both with $r = 0.71$ and residual variances of 0.22 and 0.25, respectively, though neither are as good a tracer as the $^{13}\text{CO}(2-1)/^{12}\text{CO}(1-0)$ relation from Figure 10(c).

The ratios of (2-1)/(1-0) shown in Figure 11 are greater than unity for many of the clumps. This could happen if the lines are optically thin and the gas is hot, allowing the (2-1) lines to be excited. This is consistent with the results of the LTE mass estimate with (1-0) lines being an overestimate, which would require optically thin lines. The clumps with the high (2-1)/(1-0) ratios may have an embedded source of internal heating.

As in Figure 10, we indicate the clumps that have at least one associated YSO as blue instead of black. Again in these plots, the presence of YSOs seems to have no strong relation to the trends, except that all clumps that have $^{13}\text{CO}(2-1)/^{13}\text{CO}(1-0) > 1$ do have at least one associated YSO. This is not the case for $^{12}\text{CO}(2-1)/^{12}\text{CO}(1-0)$.

We also show in Figure 11 the values for individual pixels. In all panels, the correlations of the pixels are much weaker than that of the clump-averaged values, having correlation coefficients of -0.15 , 0.49 , -0.01 , and 0.52 , respectively, for panels (a)–(d). This indicates that these trends are most accurate when averaged over the whole clump.

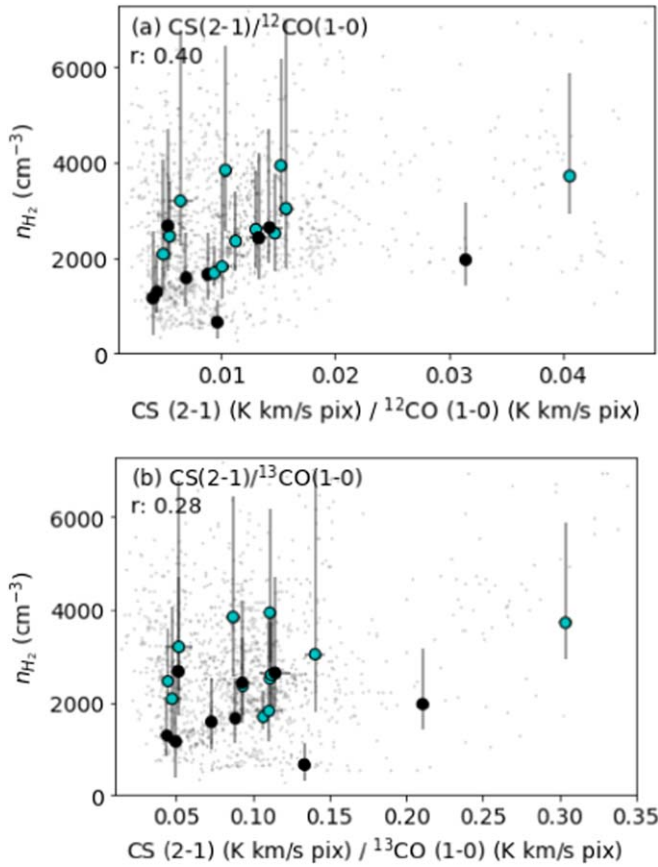


Figure 12. Density fitted by RADEX against ratios of CS(2-1) to $^{12}\text{CO}(1-0)$ (top) and to $^{13}\text{CO}(1-0)$ (bottom). CS(2-1)/ $^{12}\text{CO}(1-0)$ has a stronger correlation with density than CS(2-1)/ $^{13}\text{CO}(1-0)$ with correlation coefficients of $r = 0.40$ and $r = 0.28$, respectively. The small black points show the values of individual pixels, which have slightly weaker trends than the clump-averaged values. Despite the high critical density of CS, neither of the ratios are as strong as most of the trends of density with CO line ratios shown in Figures 10 and 11. This could be due to molecular abundance variations or because of the scales traced by the CO in the RADEX fitting. Plot symbols are the same as in Figure 9.

6.3.3. Dense Gas Tracer, CS(2-1)

CS is a commonly observed dense gas tracer in molecular clouds with an optically thin critical density of 10^5 cm^{-3} at 20 K for CS(2-1) (Shirley 2015). We examine here how the ratios of CS(2-1) to CO correlate with the RADEX-fitted density.

Figure 12 shows the ratio of the integrated intensities across a clump in units of $\text{K km s}^{-1} \text{ pix}$ of CS(2-1) to $^{12}\text{CO}(1-0)$ and CS(2-1) to $^{13}\text{CO}(1-0)$. For both ratios, there is a weak linear trend with n_{H_2} , with correlation coefficients of $r = 0.40$ and $r = 0.28$ for the ratio with $^{12}\text{CO}(1-0)$ and $^{13}\text{CO}(1-0)$, respectively. This demonstrates that CS(2-1)/ $^{12}\text{CO}(1-0)$ may be a slightly better indicator of density than CS(2-1)/ $^{13}\text{CO}(1-0)$.

We also show in Figure 12 the values of individual pixels, which have slightly weaker correlations with $r = 0.35$ and $r = 0.26$, respectively. We also indicate clumps that have at least one associated YSO as blue instead of black circles, which shows that YSO presence appears to have no effect on these trends.

Despite the high critical density of CS, Figure 12 suggests that CS(2-1) cannot predict the density as strongly as most ratios of ^{13}CO to ^{12}CO shown in Figure 10 or the ratios of excitation levels shown in Figure 11(b) and (d). This could be because of variations in molecular abundance that influence the

strength of the CS emission in addition to the density. This could also be because the RADEX fitting is primarily tracing the CO density at scales of 1–2 pc, while the CS emission may be coming from more compact cores within the clumps. With higher-resolution multiline observations and parameter fitting, we may begin to see more correlation between the fitted density and the CS emission.

7. Trends with Star Formation

7.1. Trend with Fitted Density

We looked for correlations between any of the derived quantities from Section 4.2 and star formation. Our measures of star formation for a clump are the number of YSOs associated with it and their masses (Section 5). We use a Pearson correlation coefficient, r , to evaluate how strong a relation there is between the two variables, though we acknowledge that a linear trend may not best describe the expected relationship between the variables. For that reason, we are more interested in the relative values of the correlation coefficients than the absolute values.

By far the strongest correlation of YSO presence is with the mass-weighted RADEX-fitted volume density, n_{H_2} . The density appears correlated with the number of YSOs associated with each clump ($r = 0.60$), the total mass of all YSOs associated with the clump ($r = 0.62$), and even the average mass of YSOs associated with the clump ($r = 0.63$). Figure 13 shows that clumps fit with a higher n_{H_2} have more associated YSOs, and more massive associated YSOs, and that clumps with lower values of n_{H_2} have no associated YSOs, or less massive YSOs.

7.2. Other Common Star Formation Tracers

We investigated whether or not a threshold or trend appears in other, more commonly or easily observed properties: the mean volume density ($\bar{n} = 3M/4\pi R^3 \mu m_{\text{H}_2}$, corrected to match the filling factor scale of n_{H_2} by dividing \bar{n} by $f^{3/2}$), the ratio of the integrated intensities of CS(2-1) to $^{12}\text{CO}(1-0)$, the gas surface density ($\Sigma = M/\text{Area}$), and the virial parameter, α_{vir} . The gas surface density is directly proportional to N_{H_2} and A_V , which are cited as showing star formation thresholds (i.e., Kennicutt 1998; Lada et al. 2010). The relations between these four parameters and the total mass of associated YSOs, as well as with the fitted density, n_{H_2} , are shown in Figure 14.

7.2.1. Mean Density

The mean density (Figures 14(a) and (b)) does not show much of a trend with the total mass of associated YSOs ($r = 0.37$) and shows almost no trend with the fitted density ($r = 0.06$). Figure 14(b) shows a line indicating a one-to-one correlation between mean density and fitted density, and the fitted density is almost always larger than the mean density. This is expected since the mean density is an average over the whole clump, while the fitted density is a mass-weighted average. Since more of the clump's mass is in the denser regions, the fitted density is higher. The mass weighting also means the fitted density depends on the internal structure and density profile of the clump, while the mean density contains none of that information.

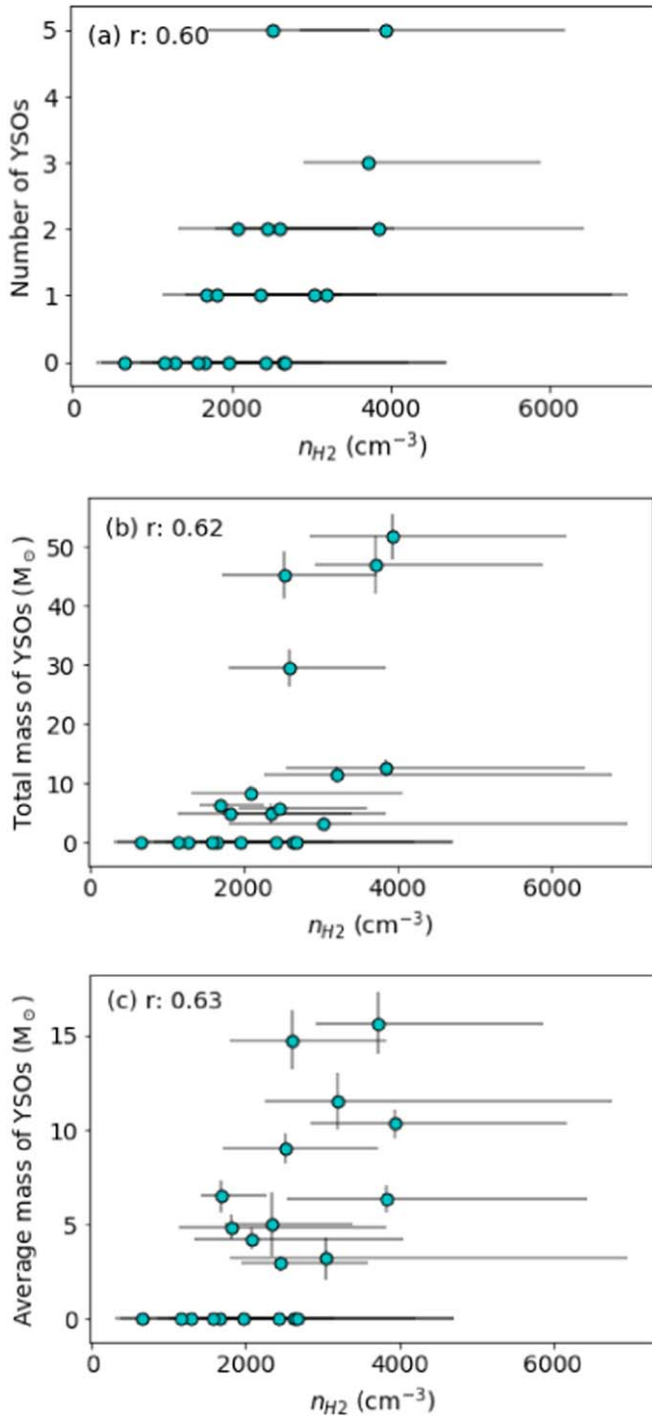


Figure 13. The number of YSOs associated with a given clump (top), their total mass (middle), and their average mass (bottom) plotted against the RADEX-fitted volume density, n_{H_2} . These three trends have correlation coefficients of 0.60, 0.62, and 0.63, respectively. The RADEX-fitted volume density had the strongest correlation with YSO presence of any parameter we considered, including the properties derived in Section 4.2 and several common star formation tracers.

7.2.2. Dense Gas Ratio

The ratio of dense gas tracers with critical densities above 10^4 cm^{-3} (e.g., HCN, HCO^+ , CS) to CO is often used as a tracer of the star formation rate in galaxies (Gao & Solomon 2004; Wang et al. 2011; Zhang et al. 2014; Li et al. 2021). In Section 6.3.3, we examined how ratios of CS(2-1) to

CO correlated with RADEX-fitted density and found that CS(2-1)/ $^{12}\text{CO}(1-0)$ shows a slightly stronger correlation with n_{H_2} than CS(2-1)/ $^{13}\text{CO}(1-0)$, though neither ratio is as good a predictor of n_{H_2} as most of the ratios between CO lines (Sections 6.3.1 and 6.3.2).

In Figures 14(c) and (d), we see that the ratio of CS(2-1)/ $^{12}\text{CO}(1-0)$ shows the strongest correlation with the RADEX-fitted density of the star formation-tracing parameters ($r = 0.40$) and an even stronger correlation with associated YSO presence ($r = 0.47$), although this is still not as strong a correlation as with fitted density (Figure 13). This measurement is difficult to relate to other observations since it cannot be directly compared with dense gas ratios of other common dense gas tracers, such as HCN or HCO^+ .

The two clumps in Figures 14(c) and (d) that have much larger CS(2-1)/ $^{12}\text{CO}(1-0)$ ratios than the rest are clumps 4 and 5, which have particularly bright CS(2-1) emission in Figure 2. It is not immediately clear what is causing this enhanced CS(2-1) emission in the region, since it does not appear particularly unique in any of the fitted physical conditions (see Figure 6). The enhanced CS emission could be related to variations in the molecular abundance of CS across the region. It also could be that the region would appear more unique at higher resolutions where dense cores would be detected and not convolved with the surrounding more diffuse gas.

7.2.3. Surface Density

Gas surface density, Σ_{gas} , is one of the most commonly used star formation threshold measures. It is correlated with star formation rate via the Kennicutt–Schmidt Relation on several scales (see reviews in Kennicutt & Evans 2012; Elmegreen 2018). One of the most commonly cited star formation thresholds is $A_V > 8$ from Lada et al. (2010), which corresponds to $\Sigma_{\text{gas}} > 116 M_{\odot} \text{ pc}^{-2}$ in their sample of Milky Way clouds.

In the LMC, Dobashi et al. (2008) found a global relation of $\frac{A_V}{N_{\text{H}}} = 1.7 \times 10^{-22} \text{ mag/H cm}^2$, although this value varies from $2.5 \times 10^{-22} \text{ mag/H cm}^2$ near 30 Dor, to $0.63 \times 10^{-22} \text{ mag/H cm}^2$ near the outskirts of the LMC. Assuming that all of the hydrogen in the Ridge is molecular, a threshold of $A_V > 8$ corresponds to $N_{\text{H}_2} > 2.4 \times 10^{22} \text{ cm}^{-2}$, based on the global estimate, and this in turn corresponds to a gas surface density of $\Sigma_{\text{gas}} > 490 M_{\odot} \text{ pc}^{-2}$, with a lower limit of $\Sigma_{\text{gas}} > 330 M_{\odot} \text{ pc}^{-2}$ based on $\frac{A_V}{N_{\text{H}}}$ measured in the outskirts of the LMC.

The threshold of $A_V > 8$ from Lada et al. (2010) was measured on $\sim 0.1 \text{ pc}$ scales, so at $45''$ (11 pc) resolution, a threshold of $490 M_{\odot} \text{ pc}^{-2}$ would correspond to $\sim 4.5 M_{\odot} \text{ pc}^{-2}$ if all of the emission is coming from compact sources with no diffuse component. The smallest gas surface density measured for a clump in the Ridge with an associated YSO is $\Sigma = 10 M_{\odot} \text{ pc}^{-2}$, and since a diffuse envelope is likely, this would be consistent with the $A_V > 8$ star formation threshold on smaller scales.

The surface density shows the weakest correlation with the presence of YSOs ($r = 0.06$) and weak, surprisingly negative correlation with fitted density as well (-0.31) (Figures 14(e) and (f)). There are clumps with high surface density and no associated YSOs, and clumps with low surface density in the Ridge that do have associated YSOs.

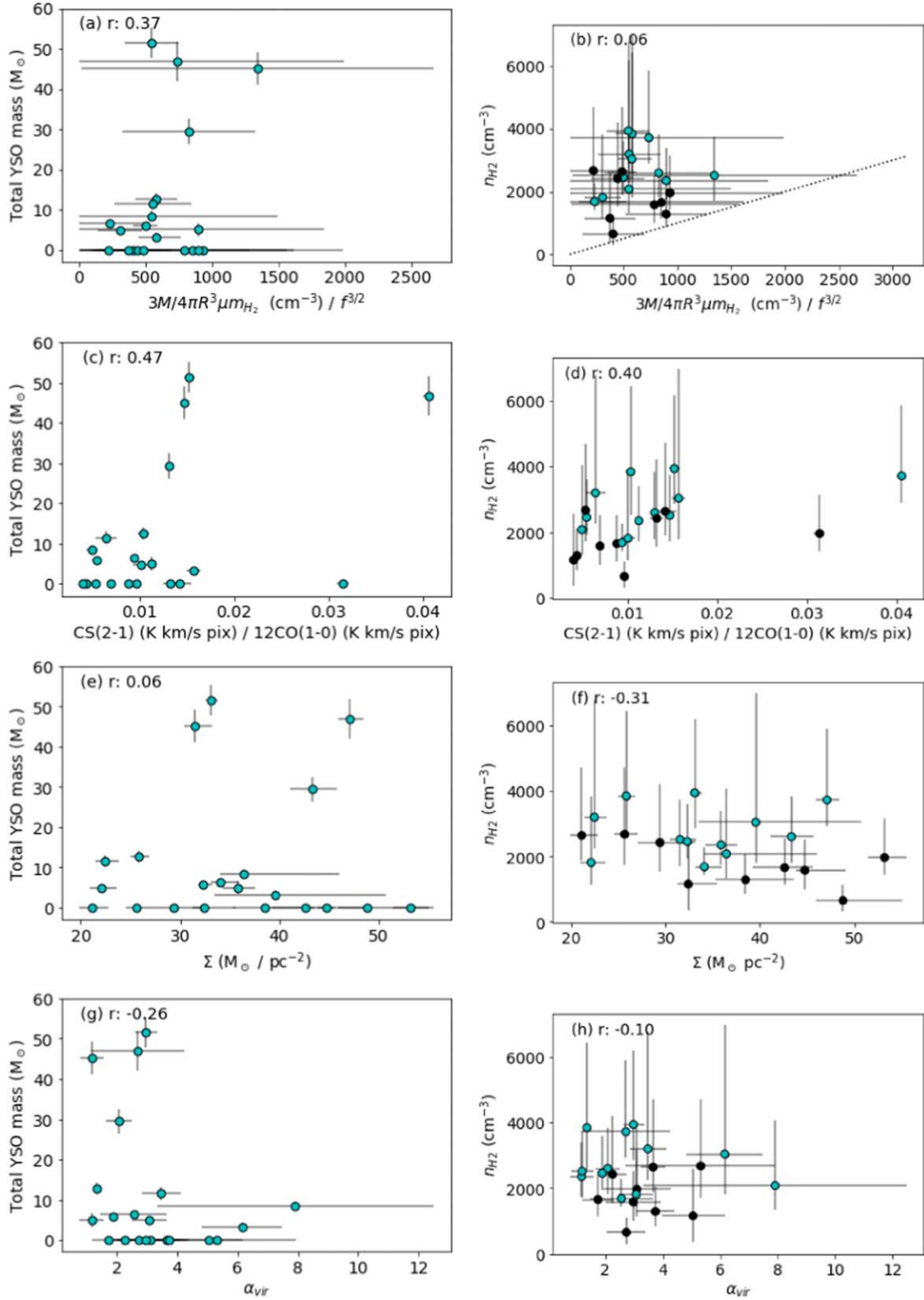


Figure 14. Left column: the total mass of YSOs associated with a clump plotted against four parameters commonly used as indicators or thresholds for stars formation: the mean density, the dense gas fraction, the gas surface density, and the virial parameter α_{vir} . Right column: the same four parameters, plotted against the fitted density, n_{H_2} . The density is the most correlated with total YSO mass, with a correlation coefficient of $r = 0.62$ (Figure 13). None of the other parameters show as strong a correlation, with CS(2-1)/ $^{12}\text{CO}(1-0)$ having the second-closest relation with $r = 0.47$. In panel (b), the dotted line shows a one-to-one correlation between the fitted and mean densities. All clumps appear consistent with having a higher fitted density than mean density, as expected. The blue points indicate clumps that have at least one associated YSO, while the black points have no associated YSOs.

7.2.4. Virial Parameter

The last metric we considered is the virial parameter, α_{vir} , calculated as

$$\alpha_{\text{vir}} = \frac{5\sigma_v^2 R}{GM}, \quad (7)$$

where R in this equation is 1.91 times the σ_R reported in Table 3 to get an “effective radius” (Solomon et al. 1987). This parameter indicates whether or not the clumps are in virial equilibrium. The correlation between α_{vir} and associated YSOs is weak, but negative as we would expect, since clumps with a high α_{vir} are less prone to collapse ($r = -0.26$; Figure 14(g)). Clumps with a high α_{vir} have a few associated YSOs, but clumps with a low α_{vir} seem to have the most massive associated YSOs. Plotting α_{vir} against fitted density shows almost no trend ($r = -0.1$; Figure 14(h)).

7.3. Discussion of Density Correlation

The correlation with RADEX-fitted density and YSO presence could indicate a threshold density for star formation, which is commonly invoked in theories of star formation (Evans 1999, and references therein). Typically, density thresholds measured in the Milky Way are $n_{\text{H}_2} > 10^4 - 10^5 \text{ cm}^{-3}$ (Evans 1999), though these are often measured on scales of ~ 0.1 pc. Since the densities in the Ridge are measured on scales of $4''$ – $9''$ (1–2 pc) depending on the filling factor, finding clumps with associated YSOs and densities of $\gtrsim 10^3 \text{ cm}^{-3}$ is not inconsistent with these Milky Way density threshold measurements. However, with a detection limit for YSOs around $\sim 2.5 M_{\odot}$ and a trend with YSO mass, there could be lower-mass, undetected YSOs associated with the lower-density clumps as well. Also, the trends we see in Figure 13 appear more continuous, rather than like the step-function that would be expected of a strict density threshold.

To understand other star formation thresholds that have been observed, we need to relate the actual physical conditions of the gas to the observational measurements we use to describe them, which are usually only projections of those conditions. The strong correlation of our RADEX-fitted density with the presence of YSOs may indicate that the fitting more directly measures the actual physical condition of the gas than any of the other parameters tested in Figure 14. Unlike measurements of mean density or surface density, the fitting allows us to probe the conditions of the gas that is the source of the emission, without being as affected by line-of-sight effects or optical depth.

Khullar et al. (2019) find in their simulations that while a high n_{H_2} is necessary for efficient star formation, typical star formation thresholds such as surface density do not actually correspond to that physical threshold. It seems like the virial parameter, α_{vir} ought to probe the actual physical conditions and be a good predictor of star formation and collapse; however, most measured α_{vir} use Equation (7), which depends on the total mass and estimations of the radius of clouds that are not symmetric or spherical. The resulting measurement is subject to the same projection effects and averaging as measuring the mean density instead of the fitted density.

While the fitted density seems to be a better predictor of star formation than any of the other measurements, we cannot directly relate that to the conditions of the clouds when they actually formed the associated YSOs, or whether those are even

the same clouds that we are observing now. Furthermore, there are many other factors that determine whether or not a cloud will form stars, and it seems unlikely that there is a single one-size-fits-all density threshold that guarantees the formation of stars, as discussed in Elmegreen (2018).

What we are seeing in Figure 13 is more likely an indicator of the local environment in the Ridge, and what density is required for the molecular gas to form stars above $\sim 2.5 M_{\odot}$ when averaged over ~ 1 pc. It would be interesting to test if the Ridge is forming fewer massive stars than regions to the north because the densities in the Ridge are lower, or if the threshold for forming stars is higher, making it more difficult to form stars than in other regions of the LMC. If the Ridge is more turbulent or more magnetically supported, it could raise the density threshold compared to other regions.

As shown in Figure 14, we cannot accurately compare this fitted density by measuring the mean density, surface density, dense gas ratio, or α_{vir} . However, as we saw in Section 6.3, ratios of ^{13}CO to ^{12}CO do show a strong correlation with the fitted gas density. We cannot easily say how those trends or specific numbers translate to other regions or size scales though, since the trend is likely dependent on the excitation and optical depth of the observed lines, and a full non-LTE analysis like the one presented here would be necessary. To make a robust comparison of star formation in the Ridge to other massive-star-forming regions in the LMC, we would need to perform the full RADEX-fitting process described in this work in other regions of the LMC. Such a study could give insights into whether the Ridge has lower densities on average compared to those regions or whether stars in those regions are able to form at lower densities, suggesting that the gas density required for star formation to occur may depend on galactic environment.

Indebetouw et al. (2013) published fluxes of $^{12}\text{CO}(2-1)$ and $^{13}\text{CO}(2-1)$ at < 1 pc resolution for 103 clumps they identified in the region of 30 Dor. The ratios of $^{13}\text{CO}(2-1)/^{12}\text{CO}(2-1)$ for those clumps ranged from 0.05 to 0.46, where the clumps in the Ridge range from 0.06 to 0.14. Furthermore, Indebetouw et al. (2013) flag six of those clumps as being associated with YSOs or clusters. These six clusters have $^{13}\text{CO}(2-1)/^{12}\text{CO}(2-1)$ ratios that range from 0.14 to 0.22. These are higher than the ratios for most of the Ridge clumps, though they are not the highest ratios of the clumps measured in 30 Dor. If the numbers from the trend in Figure 10 hold in 30 Dor and at smaller size scales, this could indicate that 30 Dor does indeed have higher densities than in the Ridge. To be sure how these two regions compare in densities though, we intend to perform our RADEX fitting on observations at a similar resolution.

8. Conclusions

We present new observations of the Molecular Ridge in the LMC, including $^{13}\text{CO}(1-0)$ and $\text{CS}(2-1)$ from ALMA at $16''$ resolution, and $^{12}\text{CO}(2-1)$ and $^{13}\text{CO}(2-1)$ from APEX at $30''$ resolution, as well as archival $^{12}\text{CO}(1-0)$ from MAGMA at $45''$ resolution. We analyzed these observations by fitting them to RADEX models and assessed how well this fitting technique was able to recover T_{kin} , N_{CO} , and n_{H_2} from simulated line emission. The results are summarized below:

1. We were able to reliably recover T_{kin} , n_{H_2} , and N_{CO} from simulated line emission by using a combination of the

95% confidence interval and 1.0 Bayesian interval. The performance of the fitting varied across the range of T_{kin} , n_{H_2} , and N_{CO} that we tested, and is dependent on the expected rms error in the line observations. We also determined that dropping one of the four lines— $^{12}\text{CO}(1-0)$, which had the lowest resolution—would result in a significant loss of fitting sensitivity, especially in moderate values of N_{CO} . We found that it was unnecessary to account for sharp boundaries between clumps, as fitting Gaussian line profiles did not change the results significantly.

2. LTE calculations from the (2-1) lines result in much lower clump masses than the RADEX fitting, which implies that the lines are sub-thermally excited and the excitation temperatures of $^{12}\text{CO}(2-1)$ and $^{13}\text{CO}(2-1)$ are not equal. When calculating LTE masses from the (1-0) lines, the masses are higher than the RADEX fitting. This could happen if the ^{12}CO lines are actually optically thin rather than thick or if the adopted beam filling factor was too large, though the relative effects of the filling factor are nonlinear and difficult to predict.
3. We calculated a value for X_{CO} in the Ridge based on the RADEX-fitted masses, getting $X_{\text{CO}} = 1.8 \times 10^{20} \text{ cm}^{-2} / (\text{K km s}^{-1})$, which is lower than we would expect for the LMC with one-third solar metallicity. This could be because the non-LTE fitting is better tracing the molecular mass or because the abundance ratio of $\text{H}_2/^{13}\text{CO} = 2 \times 10^6$ that we used was too low. We also calculated a value for $X_{^{13}\text{CO}}$, where the total N_{H_2} is related to the integrated flux of $^{13}\text{CO}(1-0)$ rather than $^{12}\text{CO}(1-0)$. We get $X_{^{13}\text{CO}} = 1.6 \times 10^{21} \text{ cm}^{-2} / (\text{K km s}^{-1})$, and the correlation is much tighter than it is with ^{12}CO . This indicates that using $^{13}\text{CO}(1-0)$ for mass estimates would be more accurate than using $^{12}\text{CO}(1-0)$.
4. The ratio $^{13}\text{CO}(2-1)/^{12}\text{CO}(1-0)$ had the tightest trend with the RADEX-fitted gas density, n_{H_2} , though all ratios of ^{13}CO to ^{12}CO fluxes are diagnostic of the volume density to a lesser extent. Ratios of upper level transitions to lower ($^{12}\text{CO}(2-1)/^{12}\text{CO}(1-0)$) are also correlated with density and not kinetic temperature. These relations are likely due to the observed lines being sub-thermally excited, so the density of the gas is important for excitation, and the excitation temperature is lower than the kinetic temperature. Six clumps had a $^{12}\text{CO}(2-1)/^{12}\text{CO}(1-0)$ ratio greater than 1 in units of pix, meaning that the ^{12}CO may actually be optically thin and relatively hot in some clumps, allowing $^{12}\text{CO}(2-1)$ to be brighter than $^{12}\text{CO}(1-0)$. The $^{13}\text{CO}(2-1)/^{13}\text{CO}(1-0)$ ratios were above 1 for eight clumps, and all eight clumps have an associated YSO, which could be a source of heating to excite the (2-1) line. We also find that neither the ratio of $\text{CS}(2-1)/^{12}\text{CO}(1-0)$ nor $\text{CS}(2-1)/^{13}\text{CO}(1-0)$ show as strong a correlation with density as most of the $^{13}\text{CO}/^{12}\text{CO}$ or (2-1)/(1-0) ratios, despite CS being commonly used as a dense gas tracer.
5. We find that no star formation parameter that can be calculated from simple mass estimates, like the mass based on an X-factor, showed a strong trend with star formation. Rather, the strongest predictor of the presence of YSOs associated with a clump was its RADEX-fitted gas density, n_{H_2} . This fitted density is correlated with the number of associated YSOs, as well as the total and average mass of those YSOs. The simpler parameters we investigated were the mean density calculated from total

mass and size, the ratio of the dense gas tracer $\text{CS}(2-1)$ to $^{12}\text{CO}(1-0)$, the surface density (which is directly related to A_V and N_{H_2}), and the virial parameter, α_{vir} . The correlation of n_{H_2} with YSO presence demonstrates that the RADEX fitting may better probe the physical conditions of the gas on these scales, though the actual relationship between the fitted density and some critical “threshold” density required for star formation is uncertain.

6. We hypothesize that the Molecular Ridge may not be actively forming massive stars as much as the northern regions either because its gas density is lower than those other regions or because it has a higher density threshold for stars to form. A higher density threshold could be due to turbulent or magnetic support, for example. The results of this study show that the RADEX-fitted volume density of the gas cannot be traced accurately by easily measured observables, such as surface density or a global mean density. While ratios of ^{13}CO to ^{12}CO are diagnostic of gas density, the scaling of this relationship is likely dependent on the local physical conditions and may not be accurate for determining relative gas density in other regions. To test these hypotheses, we will conduct a follow-up study of other active star-forming regions in the LMC with the RADEX-fitting method presented here.

We thank the anonymous referee, whose helpful comments improved this manuscript. This research is supported by NSF grants 1413231 and 1716335 (PI: K. Johnson) and NSF AAG award AST 1312902 to U. Virginia (PI: R. Indebetouw). This material is based upon work supported by the National Science Foundation Graduate Research Fellowship Program under grant No. 1842490. Any opinions, findings, and conclusions or recommendations expressed in this material are those of the author(s) and do not necessarily reflect the views of the National Science Foundation. T.W. acknowledges support from the NSF through grant AST-2009849. This work was supported by NAOJ ALMA Scientific Research grant No. 2016-03B.

This paper makes use of the following ALMA data: ADS/JAO.ALMA#2012.1.00603.S., ADS/JAO.ALMA#2015.1.00196.S., and ADS/JAO.ALMA#2017.1.00271.S. ALMA is a partnership of ESO (representing its member states), NSF (USA) and NINS (Japan), together with NRC (Canada), NSC and ASIAA (Taiwan), and KASI (Republic of Korea), in cooperation with the Republic of Chile. The Joint ALMA Observatory is operated by ESO, AUI/NRAO and NAOJ. The National Radio Astronomy Observatory is a facility of the National Science Foundation operated under cooperative agreement by Associated Universities, Inc.

Based on observations with the Atacama Pathfinder EXperiment (APEX) telescope. APEX is a collaboration between the Max Planck Institute for Radio Astronomy, the European Southern Observatory, and the Onsala Space Observatory. Swedish observations on APEX are supported through Swedish Research Council grant No. 2017-00648.

Facilities: APEX, ALMA.

Software: Pipeline-CASA51-P2-B v.40896 (Davis 2021, in preparation), CASA (v.5.1.1-5, v.5.6.1; McMullin et al. 2007), RADEX (van der Tak et al. 2007), quickclump (Sidorin 2017), Astropy (Astropy Collaboration et al. 2013), Matplotlib (Hunter 2007), NumPy (Harris et al. 2020), SciPy (Virtanen et al. 2020).

Appendix A Beam Filling Factor

A filling factor (defined as $f = T_{B,45''}/T_{B,true}$) is required to get accurate physical conditions. We attempted two methods of dealing with this issue: fitting the filling factor as a fourth dimension in the fitting process, and fitting ratios of the intensities rather than their absolute values to avoid the need for the filling factor at all. However, both of these methods reduce the degrees of freedom in the fitting to zero, and we found they were unable to constrain the physical parameters or the beam filling factor reliably.

There are two common types of results when fitting the filling factor. An example of the first of these is shown in Figure 15, using the same representative data as in Figure 5 that has a high signal-to-noise ratio (ranging from 5 for $^{13}\text{CO}(2-1)$ to 16 for $^{12}\text{CO}(1-0)$). In this plot, the filling factor is not constrained, and the four-dimensional probability distribution is multimodal. This results in a maximum likelihood point in four-dimensional parameter space (the blue line in Figure 15) that is inconsistent with the maximum of the collapsed

probability profile for the filling factor (the orange line in Figure 15), making the results difficult to interpret.

The other common behavior when fitting the filling factor is shown in Figure 16 using the peak of one of the fainter clumps (numbered 21 in Figure 7). In this case, the filling factor is well constrained on a low value, but the resulting fit for the other parameters is highly unlikely to occur physically. The temperature is poorly constrained but pushed to high temperatures, and N_{CO} is extremely high and n_{H_2} is low, which would require a very long path length along the line of sight ($\gtrsim 80$ pc), which is inconsistent with the size of the clump being fitted (~ 10 pc). We conclude that this type of result is unphysical and unreliable, so cannot be used to determine the filling factor.

Fitting ratios from the four observations removes the filling factor from the equation entirely, assuming that all four lines are tracing the same gas with the same filling factor. However, one line must be selected as the denominator, and so the number of data points to fit is reduced to three. The resulting fit has the same issues as fitting the filling factor: either the parameters are poorly constrained or the constrained values are

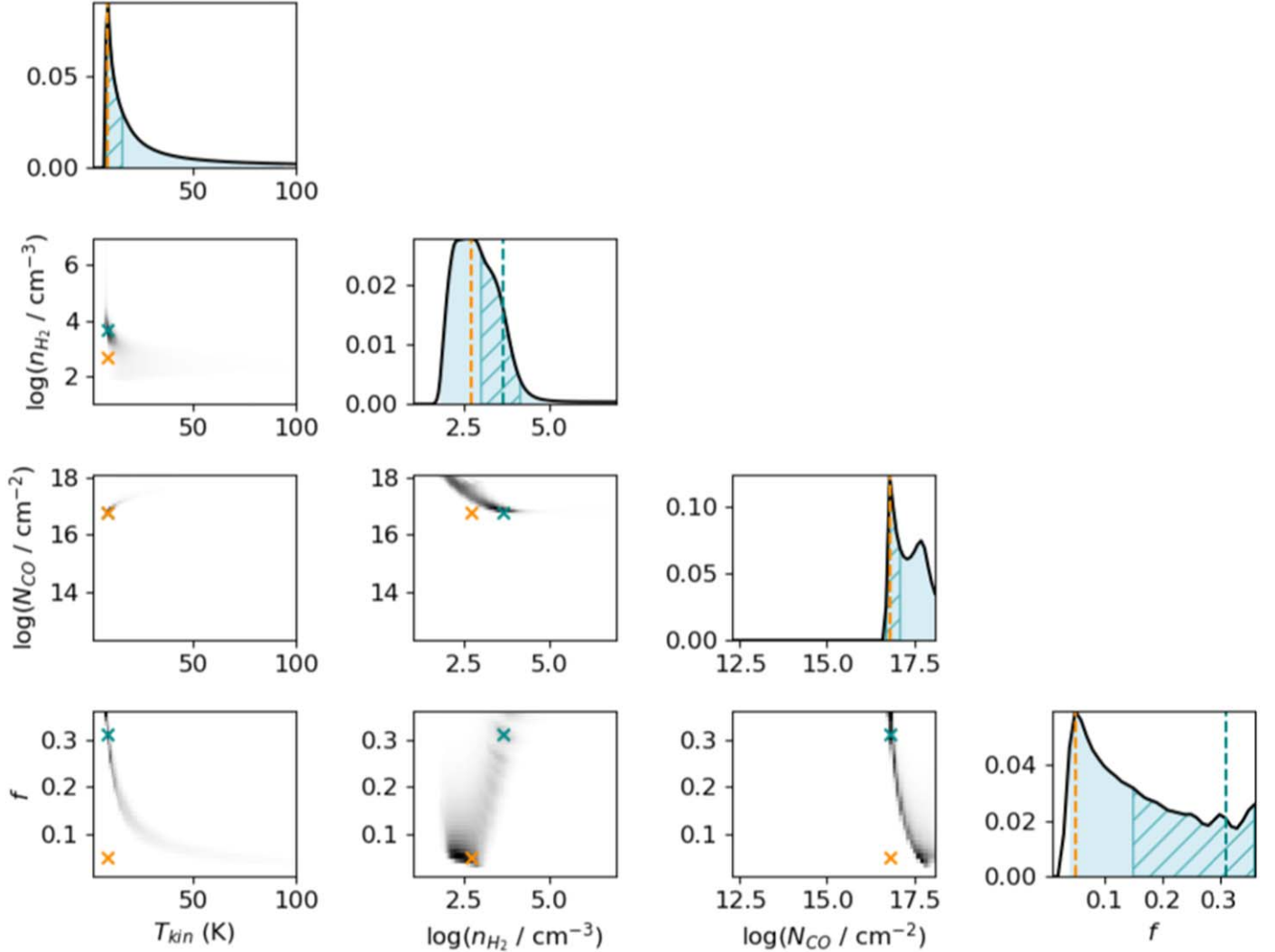


Figure 15. Example of a probability distribution from representative data (1.7 K, 0.2 K, 1.2 K, and 0.14 K for $^{12}\text{CO}(1-0)$, $^{13}\text{CO}(1-0)$, $^{12}\text{CO}(2-1)$, and $^{13}\text{CO}(2-1)$, respectively; same data, shading, and lines as in Figure 5) with the beam filling factor, f , added as a fourth dimension to fit, with $R_{13} = 100$. This results in a poorly constrained filling factor and a multimodal four-dimensional probability distribution. The multimodality of the probability distribution results in a major inconsistency between the peak of the four-dimensional probability distribution and the peak of the collapsed probability profile for the filling factor.

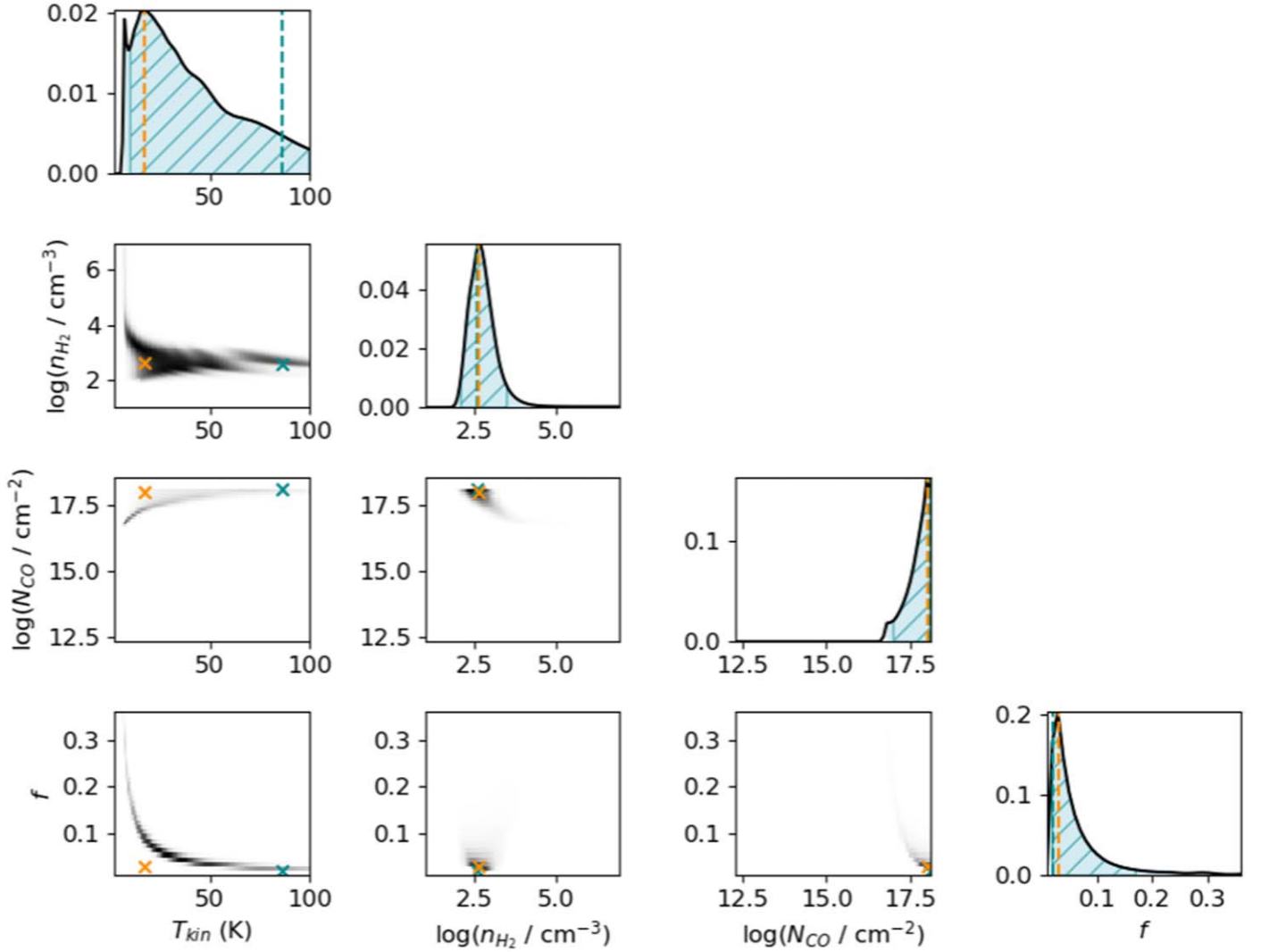


Figure 16. Example of a probability distribution from fainter data (0.96 K, 0.17 K, 0.91 K, and 0.10 K for $^{12}\text{CO}(1-0)$, $^{13}\text{CO}(1-0)$, $^{12}\text{CO}(2-1)$, and $^{13}\text{CO}(2-1)$, respectively) with the beam filling factor, f , added as a fourth dimension to fit, and with the same shading and lines as in Figure 5. This results in a well-constrained fit for the filling factor at a low value, but an unconstrained, unphysically high T_{kin} and a combination of a high N_{CO} and low n_{H_2} , which would require a much longer path length than is consistent with the size of the clump ($\gtrsim 80$ pc compared to ~ 10 pc). We consider this type of fit unreliable and unphysical.

unphysical. Figure 17 shows an example of an unphysical fit from ratio fitting, where the fitted temperature is almost entirely unconstrained and the combination of a high N_{CO} and low n_{H_2} requires a long path length that is inconsistent with the size of the clump (Figure 18).

Since fitting the filling factor or the ratios resulted in either an unreliable or unconstrained result, and because fitting the filling factor also significantly increases the computational requirements, we assumed a range of filling factors for the region, similar to our handling of R_{13} . The upper limits were determined by calculating the ratio of the high-resolution ($16''$) ALMA $^{13}\text{CO}(1-0)$ data to that same data convolved to $45''$ to get an observed upper limit.

We ran `quickclump` on the high-resolution ALMA $^{13}\text{CO}(1-0)$, then took the ratio of the peak of the 50 brightest clumps and the peak of the corresponding low-resolution clump as defined in Section 4.1. This results in an upper limit for the filling factor of these high-resolution clumps ($f < T_{B,45''}/T_{B,16''}$). Each low-resolution clump had multiple corresponding high-resolution clumps, so we looked at the minimum upper limit of those. All low-resolution clumps had

an upper limit above 20%, so we adopt an upper limit on the filling factor of 20% across the region.

The lower limit of the range comes from the fits becoming unphysical below $f \sim 10\%$. Taking lower beam filling factors results in unrealistically large temperatures with large errors, and large path lengths along the line of sight that are inconsistent with the projected size of the clumps.

We make an exception to the 10% filling factor lower limit for the clumps numbered 7, 8, and 9 in Figure 7. Each of these clumps return unphysical values similar to those shown in Figure 16 when fitted with a 10% filling factor. We show the resultant line-of-sight path length when adopting filling factors of 10%, 15%, and 20% to demonstrate the unphysical nature of the 10% results in that region. The path length is determined by dividing the H_2 column density (N_{H_2}) in units of square centimeters by the H_2 volume density (n_{H_2}) in units of cubic centimeters, and converted to parsecs. These types of unphysical values occur primarily when the fitted filling factor is too low, and so for these three clumps, we use a filling factor of 15%, which is large enough that the results are no longer unphysical.

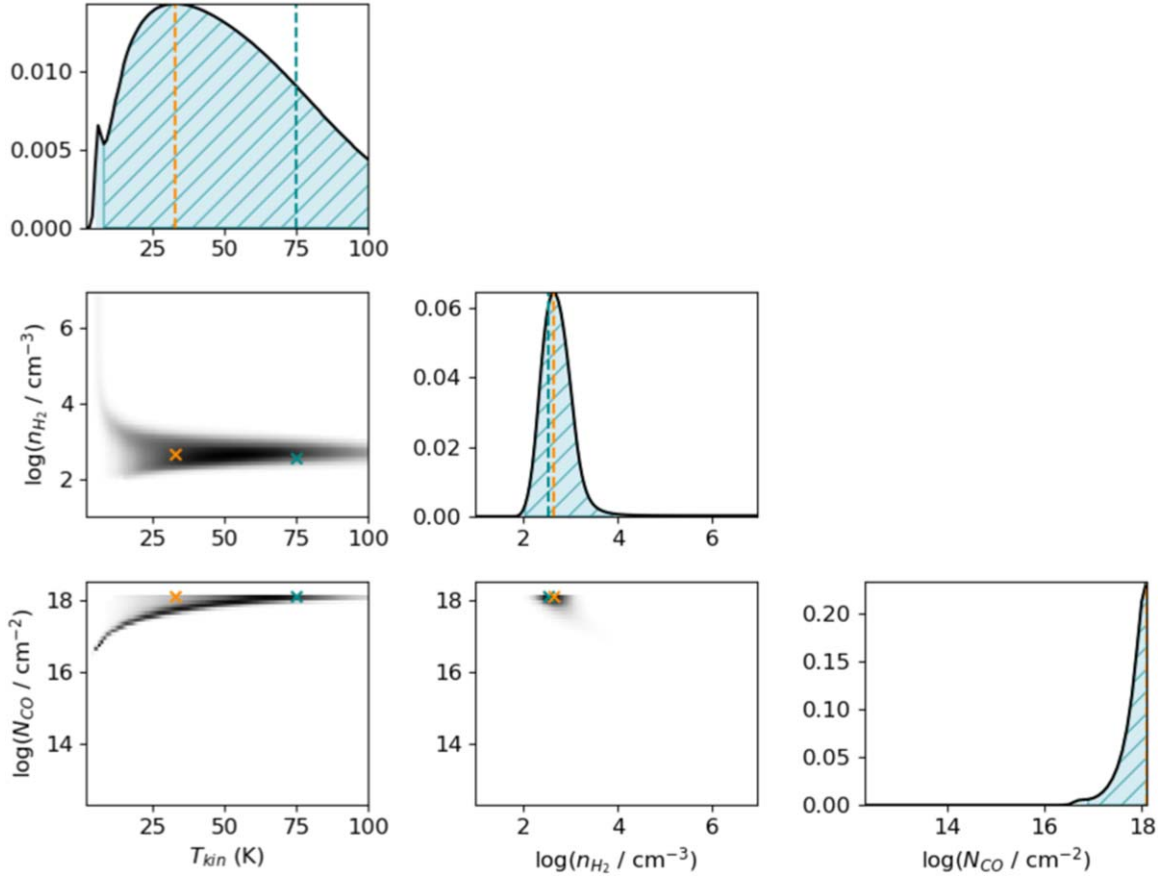


Figure 17. Example of a probability distribution from fitting the ratios of the line intensities, using $^{13}\text{CO}(1-0)$ as the denominator. This plot uses the same intensities as Figure 16, so the fitted ratios are 5.6, 5.3, and 0.59 for $^{12}\text{CO}(1-0)/^{13}\text{CO}(1-0)$, $^{12}\text{CO}(2-1)/^{13}\text{CO}(1-0)$, and $^{13}\text{CO}(2-1)/^{13}\text{CO}(1-0)$, respectively. The shading and lines are the same as in Figure 5. This results in an unconstrained, unphysically high T_{kin} and a combination of a high N_{CO} and low n_{H_2} , which would require a much longer path length than is consistent with the size of the clump ($\gtrsim 80$ pc compared to ~ 10 pc). We consider this type of fit unreliable and unphysical.

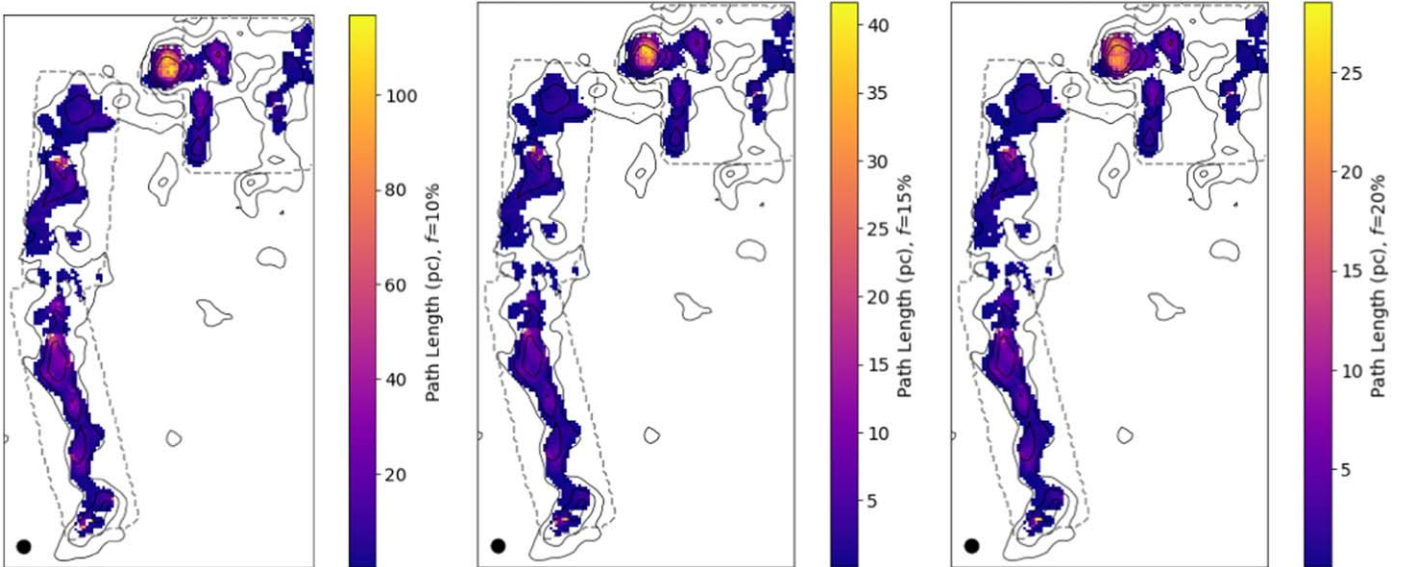


Figure 18. Line-of-sight path length of the fitting results with beam filling factors of 10%, 15%, and 20%. The path length is determined by dividing the H_2 column density in units of square centimeters by the H_2 volume density in units of cubic centimeters, and converted to parsecs. With a beam size of ~ 11 pc, the path length becomes unrealistically large around clumps numbered 7, 8, and 9 (Figure 7) when we assume $f = 10\%$, so we instead use a filling factor lower limit of 15% in that region. The contours are the $^{12}\text{CO}(1-0)$ integrated intensity as shown in Figure 2, and the dashed line is the common observation footprint.

The assumed filling factor has the strongest effect on the fitted temperature. Due to the highest-probability line for T_{kin} and f in the bottom left corner plots of Figures 15 and 16, at low

filling factors, the temperature quickly gets high with large errors, while at higher filling factors, the variation in temperature levels off at lower values and varies much less.

Because of this, taking a filling factor that is too low strongly affects the fitted temperature.

The density is also affected by the filling factor, though not nearly as strongly as temperature. A higher filling factor results in a higher density most, but not all, of the time. When reporting values of N_{CO} , we multiply the filling factor back into the results ($N_{\text{CO}} \times f$) to get an accurate mass calculation. This results in a value of N_{CO} that is almost entirely unaffected by the assumed filling factor.

Appendix B Evaluating Fitting Performance

We tested how well our multiline data with similar signal-to-noise as our Ridge measurements can be fit by this process and which of the five intervals described in Section 3.1 is best to accurately constrain the parameters (the five intervals are the three Bayesian intervals based on the three-dimensional probability distribution and the two confidence intervals based on one-dimensional probability profiles for each parameter). To do this evaluation, we simulated data for a range of physical parameters, covering the tested parameter space (T_{kin} between 5 and 55 K, n_{H_2} between $10^{2.5} \text{ cm}^{-3}$ and 10^6 cm^{-3} , and N_{CO} between $10^{14.5} \text{ cm}^{-2}$ and 10^{18} cm^{-2}). For each combination of these three parameters, we used RADEX to determine the expected emission from the four lines that we observe: $^{12}\text{CO}(1-0)$, $^{13}\text{CO}(1-0)$, $^{12}\text{CO}(2-1)$, and $^{13}\text{CO}(2-1)$. We then added random Gaussian noise based on the observed rms error for each line after convolving to a resolution of $45''$ in each cube to match the $^{12}\text{CO}(1-0)$ resolution: 0.11 K, 0.017 K, 0.1 K, and 0.035 K, respectively, for $^{12}\text{CO}(1-0)$, $^{13}\text{CO}(1-0)$, $^{12}\text{CO}(2-1)$, and $^{13}\text{CO}(2-1)$. We did not include any beam filling factors in this process.

For each combination of physical parameters, we generated 100 instances of random Gaussian noise and then determined p_{max} , Bayesian intervals, and confidence intervals for each instance (see Section 3.1 for a description of these calculations). In all cases, we used $R_{13} = 100$. We then considered how often in these 100 instances the true model values were recovered within each of the five intervals. The recovery of each parameter depends on all three parameters (e.g., N_{CO} is better recovered at higher T_{kin} , as well as at higher N_{CO}); so to compare the five intervals' performances, we examine how each parameter is recovered as a function of each of the other two parameters as well as itself.

An example of such a plot is shown in Figure 19, where we compare how often the correct value of n_{H_2} falls in each of the five intervals as a function of T_{kin} (and so collapsed over all values of n_{H_2} and N_{CO}). This shows that we do not robustly recover the true value of n_{H_2} when T_{kin} is low. Also, the 67% confidence interval is a smaller range and contains the correct answer a much lower fraction of the time than the other wider confidence intervals, which is exactly what we would expect from a 1σ confidence interval.

How often the model value is in the interval tells us how accurate our fitting is, but we also want to know how precise our fitting can be. If the interval includes the entire parameter range, the true value will always be in it, but we have also done nothing to constrain it. So, we also consider the size of each interval for each parameter, as a function of each parameter. We show an example plot of this in Figure 20, where the size of the five n_{H_2} intervals are again plotted as a function of T_{kin} . In

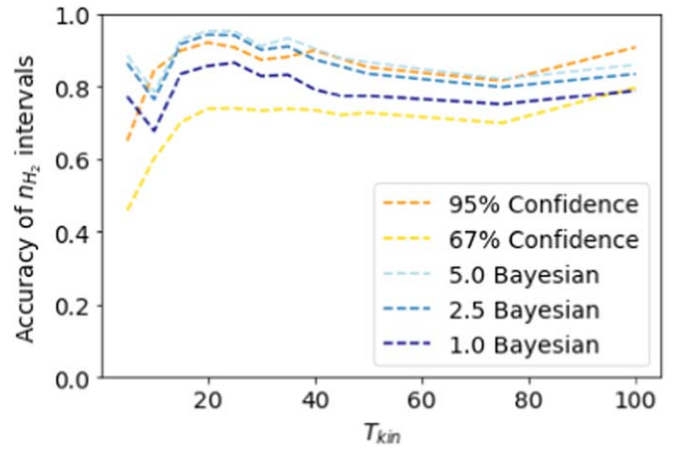


Figure 19. An example of how well we recover n_{H_2} as a function of T_{kin} . For each of the five intervals, we plot the fraction of runs in which the true model value was within the interval, averaged over all n_{H_2} and N_{CO} to get a function of T_{kin} . This plot shows that we do not robustly recover n_{H_2} when T_{kin} is low. Also, the 67% confidence interval is much less accurate than the other four intervals.

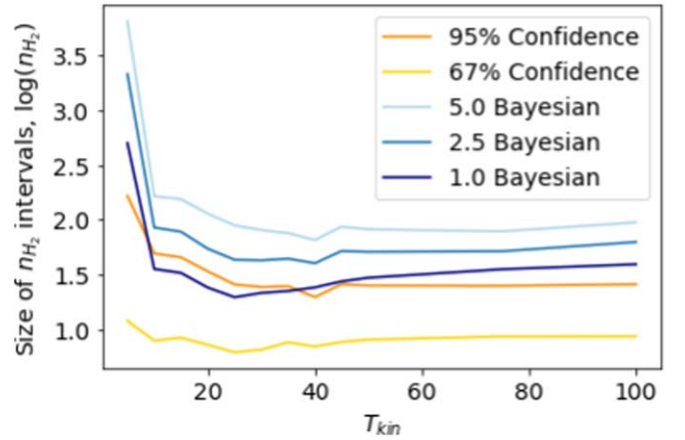


Figure 20. An example of how precise our fitting of n_{H_2} is as a function of T_{kin} . For each of the five intervals, we plot the total size of the n_{H_2} interval in dex, averaged over all n_{H_2} and N_{CO} to get a function of T_{kin} . The size shown here does not account for where within the interval the best-fit value is, and it is frequently not symmetrical. At $T_{\text{kin}} < 10 \text{ K}$, n_{H_2} is less constrained, by approximately an order of magnitude in most cases. Also, the 67% confidence interval constrains n_{H_2} most precisely (although we know from Figure 19 that it is much less accurate). Unsurprisingly, the most accurate intervals are also the least constrained.

this plot, n_{H_2} is better constrained when T_{kin} is high. As we would expect, the most constrained interval (the 67% confidence interval) is the least accurate (as shown in Figure 19), while the least constrained interval (the 5.0 Bayesian interval) is the most accurate.

From an examination of plots similar to Figures 19 and 20 for all of the parameters, the combination of the 95% confidence interval and the 1.0 Bayesian interval delivers the desired balance of accuracy and precision to fit the physical parameters to the data. There are some regions of parameter space where one is preferred over the other and vice versa, and so a combination of the two is used to fit the actual data. This is demonstrated in Figure 21, where at high N_{CO} ($> 10^{17.5} \text{ cm}^{-2}$), the 1.0 Bayesian interval returns a tight constraint on the wrong value, while the 95% confidence interval tightly constrains the

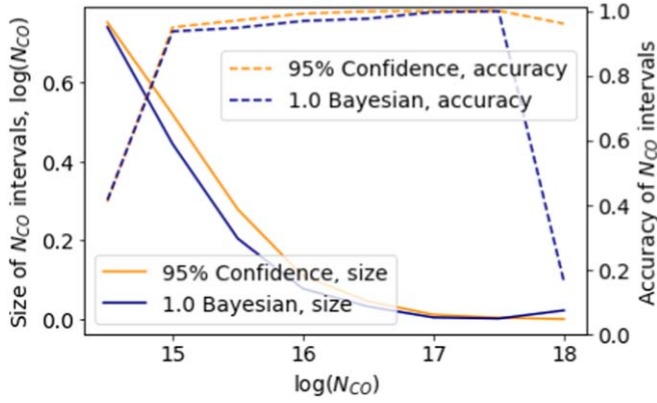


Figure 21. The accuracy and precision of the 95% confidence interval and the 1.0 Bayesian interval for N_{CO} as a function of N_{CO} (averaged over n_{H_2} and T_{kin}). At low N_{CO} , neither interval is able to accurately predict the true N_{CO} value despite the size of the interval increasing. At high N_{CO} , the Bayesian interval drops sharply in accuracy, while the confidence interval does not.

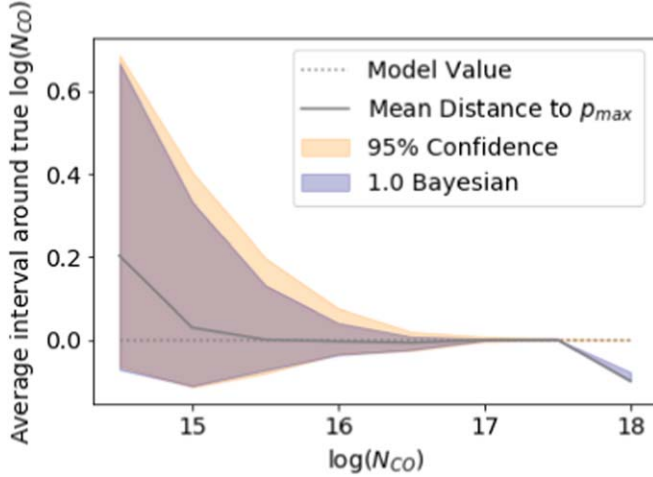


Figure 22. Offset of the 95% confidence interval, the 1.0 Bayesian interval, and p_{max} from the true value of N_{CO} , averaged over all T_{kin} and n_{H_2} , to get a function of N_{CO} . At low N_{CO} , both intervals as well as p_{max} overestimate N_{CO} . At high N_{CO} , the confidence interval is accurate and well constrained. The Bayesian interval however is precise and inaccurate—it tightly fits an underestimate.

correct value. In other regions of parameter space, the 1.0 Bayesian interval is just as accurate as the 95% confidence interval but more precise. We use a combination of the two intervals by selecting the more precise one to determine the correct value, with one exception: when the 95% interval fits a high N_{CO} value ($> 10^{17.5} \text{ cm}^{-2}$), we always use the 95% interval since Figure 21 demonstrates that the Bayesian interval cannot be trusted in this range.

We also consider systematic offsets (e.g., consistent over- or underestimates) between the model values and the fitted intervals as measured by the mean distances of the model values to the edges of the intervals. We do this for the 95% confidence interval, the 1.0 Bayesian interval, and p_{max} for each parameter as a function of each parameter. We show an example of one such plot in Figure 22. At low N_{CO} , both intervals accurately include the true N_{CO} value, but most of the interval is an overestimate, while at high N_{CO} , the 1.0 Bayesian interval underestimates N_{CO} .

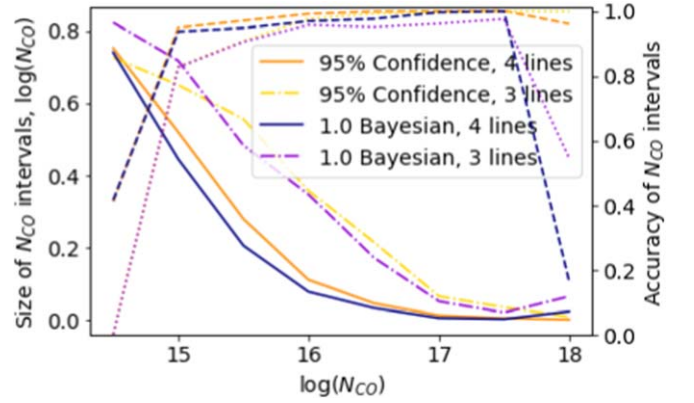


Figure 23. A comparison of how the 95% confidence interval and 1.0 Bayesian interval fit N_{CO} as a function of N_{CO} when four lines are included ($^{12}\text{CO}(1-0)$, $^{12}\text{CO}(2-1)$, $^{13}\text{CO}(1-0)$, and $^{13}\text{CO}(2-1)$), and when only three lines are included (no $^{12}\text{CO}(1-0)$). The solid lines show the sizes of the intervals, while the dashed lines show how often the true value is in the interval. Fitting with only three lines makes the biggest difference at moderate N_{CO} , where four lines can constrain the value much better than only three. At very high or very low N_{CO} , they perform similarly.

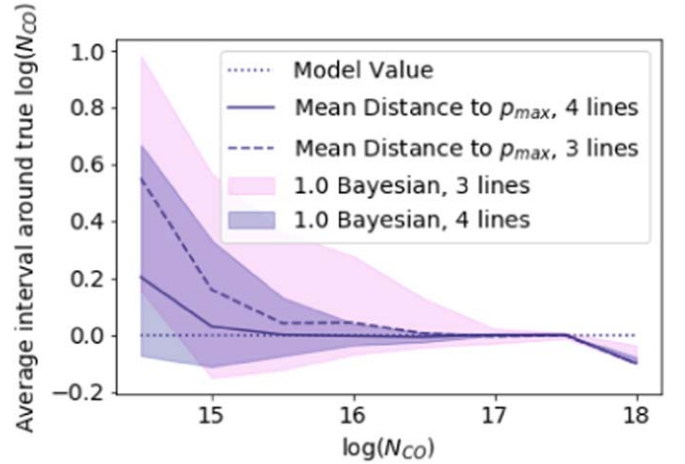


Figure 24. Offset of the 1.0 Bayesian interval and p_{max} from the true value of N_{CO} as a function of N_{CO} when four lines are included ($^{12}\text{CO}(1-0)$, $^{12}\text{CO}(2-1)$, $^{13}\text{CO}(1-0)$, and $^{13}\text{CO}(2-1)$), and when only three lines are included (no $^{12}\text{CO}(1-0)$). As in Figure 23, four lines more tightly constrain N_{CO} in general, especially at moderate values of N_{CO} . Note that at low N_{CO} , the average interval is entirely above the true value if only three lines are fitted.

B.1. Dependence on $^{12}\text{CO}(1-0)$

We tested the performance of the model fitting when we included only the highest-resolution lines: $^{13}\text{CO}(1-0)$, $^{12}\text{CO}(2-1)$, and $^{13}\text{CO}(2-1)$. We dropped the $^{12}\text{CO}(1-0)$ since it had the worst resolution at $45''$. We then simulated data once again using the RADEX model from the same range of parameter space as above. This time we added random Gaussian noise based on the error after convolving each cube to $30''$ instead of $45''$ to match the new limiting resolution of $^{13}\text{CO}(2-1)$.

We compared the fitting performance using the measures described above to determine how much sensitivity we lose by not including the information from $^{12}\text{CO}(1-0)$. We show example plots from this comparison in Figures 23 and 24. By dropping the $^{12}\text{CO}(1-0)$, we are less sensitive to intermediate N_{CO} values. While the resulting fitted intervals still include the correct value almost all of the time for $N_{\text{CO}} > 10^{15} \text{ cm}^{-2}$, they are only well constrained for $N_{\text{CO}} > 10^{16} \text{ cm}^{-2}$. Since we

expect that much of the Ridge may fall in this range of N_{CO} values, we decided that the improved sensitivity to the physical parameters is worth losing some resolution.

A comprehensive set of plots comparing the performance of fitting in the case of three lines instead of four for all parameters similar to Figures 19–24 is available as supplementary material.¹⁷

Appendix C Radex-fitting Method

In addition to the method described in Section 3.2, we tested holding T_{kin} and n_{H_2} fixed for the whole clump (clump fixed method) and fully fitting T_{kin} and n_{H_2} for every velocity and every pixel (full fit method). We decided to hold T_{kin} and n_{H_2} fixed for only the line (line fixed method, described in Section 3.2) because this had the best physical motivation and gave the most realistic results. The full fit method resulted in the line edges becoming unrealistically low in T_{kin} and high in N_{CO} and having poor fits at the line edges. The full fit method is also less consistent with the assumptions of escape probability codes including RADEX, which assumes constant excitation across a finite-sized cloud.

The clump fixed method had similar results to the line fixed method, but the N_{CO} fits were much less constrained on the edges of the clump. Also, a uniform temperature and density profile is unrealistic for a clump, and holding these values fixed for the whole clump made the fit overly dependent on the single peak pixel, which we wanted to avoid.

We compared the resulting masses, temperatures, and densities for each clump to the masses from the full fit and clump fixed methods, rather than the line fixed method. A table summarizing how our measurements would change with different fitting methods is given in Table 6, where we show the ratio of the derived mass, temperature, and density from alternate fitting methods and our preferred line fixed method, averaged across all clumps included in this analysis and the standard deviation of these ratios.

The full fit method results in mass, temperature, and density estimates that seem largely consistent with the line fixed method. The difference between these two methods is in the fitting of the line wings, and since the line wings have a much lower column density than the line peak, the mass and the mass-weighted T_{kin} and n_{H_2} are not much higher or lower than when we use the line fixed method. When using the full fit method, the lower intensities in the line wings cause the fitting to prefer lower temperatures and densities, which is compensated for with higher N_{CO} values, causing a slightly higher mass than the line fixed method.

The clump fixed method results in a lower mass and higher temperature than the line fixed method on average. The density is consistent with the line fixed method, but with larger variations. A lower mass is expected from this method, since the fitting compensates for a higher temperature by preferring a lower N_{CO} . On the edges of the clump where we would expect the temperature to be lower, it is instead fitted with the temperature from the center of the clump, causing lower N_{CO} estimates and a lower mass overall. The temperature is also expected to be higher, though the effect is not as large because T_{kin} is mass-weighted, and the center of the clump where N_{CO}












Table 6
Comparison of RADEX-fitting Methods

	M/M_{LF}	$T_{\text{kin}}/T_{\text{kin,LF}}$	$n_{\text{H}_2}/n_{\text{H}_2,\text{LF}}$
Full Fit	1.07 ± 0.09	0.92 ± 0.12	0.81 ± 0.17
Clump Fixed	0.83 ± 0.11	1.15 ± 0.14	1.04 ± 0.42

Note. Comparison of different methods of determining mass (from N_{CO}), T_{kin} or T_{ex} , and n_{H_2} . These values are the average of the ratios for all of the clumps that were fit with these methods. M_{LF} and $T_{\text{kin,LF}}$ are the values derived from the line fixed RADEX-fitting method.

is highest is less affected by the constant temperature assumption.

ORCID iDs

Molly K. Finn  <https://orcid.org/0000-0001-9338-2594>
 Remy Indebetouw  <https://orcid.org/0000-0002-4663-6827>
 Kelsey E. Johnson  <https://orcid.org/0000-0001-8348-2671>
 Allison H. Costa  <https://orcid.org/0000-0002-7408-7589>
 C.-H. Rosie Chen  <https://orcid.org/0000-0002-3925-9365>
 Akiko Kawamura  <https://orcid.org/0000-0001-7813-0380>
 Toshikazu Onishi  <https://orcid.org/0000-0001-7826-3837>
 Jürgen Ott  <https://orcid.org/0000-0001-8224-1956>
 Kazuki Tokuda  <https://orcid.org/0000-0002-2062-1600>
 Tony Wong  <https://orcid.org/0000-0002-7759-0585>
 Soroia Zahorecz  <https://orcid.org/0000-0001-6149-1278>

References

- Astropy Collaboration, Robitaille, T. P., Tollerud, E. J., et al. 2013, *A&A*, **558**, A33
 Barlow, R. 2004, arXiv:physics/0401042
 Bica, E., Claria, J. J., Dottori, H., Santos, J. F. C. J., & Piatti, A. E. 1996, *ApJS*, **102**, 57
 Bolatto, A. D., Wolfire, M., & Leroy, A. K. 2013, *ARA&A*, **51**, 207
 Brand, J., & Wouterloot, J. G. A. 1995, *A&A*, **303**, 851
 Bressan, A., Marigo, P., Girardi, L., et al. 2012, *MNRAS*, **427**, 127
 Calzetti, D., Kennicutt, R. C., Engelbracht, C. W., et al. 2007, *ApJ*, **666**, 870
 Carlson, L. R., Sewilo, M., Meixner, M., Romita, K. A., & Lawton, B. 2012, *A&A*, **542**, A66
 Castets, A., Duvert, G., Dutrey, A., et al. 1990, *A&A*, **234**, 469
 Chen, C. H. R., Indebetouw, R., Chu, Y.-H., et al. 2010, *ApJ*, **721**, 1206
 Cohen, R. S., Dame, T. M., Garay, G., et al. 1988, *ApJL*, **331**, L95
 Davies, R. D., Elliott, K. H., & Meaburn, J. 1976, *MmRAS*, **81**, 89
 Dobashi, K., Bernard, J. P., Hughes, A., et al. 2008, *A&A*, **484**, 205
 Elmegreen, B. G. 2018, *ApJ*, **854**, 16
 Evans, N. J. I. 1999, *ARA&A*, **37**, 311
 Fukui, Y., Kawamura, A., Minamidani, T., et al. 2008, *ApJS*, **178**, 56
 Gao, Y., & Solomon, P. M. 2004, *ApJ*, **606**, 271
 Gruendl, R. A., & Chu, Y.-H. 2009, *ApJS*, **184**, 172
 Harris, C. R., Millman, K. J., van der Walt, S. J., et al. 2020, *Natur*, **585**, 357
 Heikkilä, A., Johansson, L. E. B., & Olofsson, H. 1999, *A&A*, **344**, 817
 Henize, K. G. 1956, *ApJS*, **2**, 315
 Heyer, M., & Dame, T. M. 2015, *ARA&A*, **53**, 583
 Heyer, M. H., Carpenter, J. M., & Snell, R. L. 2001, *ApJ*, **551**, 852
 Hughes, A., Wong, T., Ott, J., et al. 2010, *MNRAS*, **406**, 2065
 Hunter, J. D. 2007, *CSE*, **9**, 90
 Indebetouw, R., Brogan, C., Chen, C. H. R., et al. 2013, *ApJ*, **774**, 73
 Indebetouw, R., Whitney, B. A., Kawamura, A., et al. 2008, *AJ*, **136**, 1442
 Indebetouw, R., Wong, T., Chen, C. H. R., et al. 2020, *ApJ*, **888**, 56
 Kennicutt, R. C., & Evans, N. J. 2012, *ARA&A*, **50**, 531
 Kennicutt, R. C. J. 1998, *ApJ*, **498**, 541
 Khullar, S., Krumholz, M. R., Federrath, C., & Cunningham, A. J. 2019, *MNRAS*, **488**, 1407
 Koeppen, J., & Kegel, W. H. 1980, *A&AS*, **42**, 59
 Lada, C. J., Lombardi, M., & Alves, J. F. 2010, *ApJ*, **724**, 687
 Li, F., Wang, J., Gao, F., et al. 2021, *MNRAS*, **503**, 4508
 Longmore, S. N., Bally, J., Testi, L., et al. 2013, *MNRAS*, **429**, 987
 Maddalena, R. J., & Thaddeus, P. 1985, *ApJ*, **294**, 231

¹⁷ <https://doi.org/10.5281/zenodo.4646288>

- Mangum, J. G., & Shirley, Y. L. 2015, *PASP*, **127**, 266
- McMullin, J. P., Waters, B., Schiebel, D., Young, W., & Golap, K. 2007, in ASP Conf. Ser. 376, *Astronomical Data Analysis Software and Systems XVI*, ed. R. A. Shaw, F. Hill, & D. J. Bell (San Francisco, CA: ASP), 127
- Meixner, M., Gordon, K. D., Indebetouw, R., et al. 2006, *AJ*, **132**, 2268
- Meixner, M., Panuzzo, P., Roman-Duval, J., et al. 2013, *AJ*, **146**, 62
- Mizuno, N., Yamaguchi, R., Mizuno, A., et al. 2001, *PASJ*, **53**, 971
- Nikolić, S., Garay, G., Rubio, M., & Johansson, L. E. B. 2007, *A&A*, **471**, 561
- Nishimura, A., Tokuda, K., Kimura, K., et al. 2015, *ApJS*, **216**, 18
- Padoan, P., Juvela, M., Bally, J., & Nordlund, Å. 2000, *ApJ*, **529**, 259
- Peñaloza, C. H., Clark, P. C., Glover, S. C. O., Shetty, R., & Klessen, R. S. 2017, *MNRAS*, **465**, 2277
- Robitaille, T. P. 2017, *A&A*, **600**, A11
- Robitaille, T. P., Whitney, B. A., Indebetouw, R., & Wood, K. 2007, *ApJS*, **169**, 328
- Sakamoto, S. 1994, *PASP*, **106**, 1112
- Schaefer, B. E. 2008, *AJ*, **135**, 112
- Seale, J. P., Meixner, M., Sewilo, M., et al. 2014, *AJ*, **148**, 124
- Shirley, Y. L. 2015, *PASP*, **127**, 299
- Sidorin, V. 2017, Quickclump: Identify Clumps within a 3D FITS Datacube, v1.0, Astrophysics Source Code Library, ascl:1704.006
- Skrutskie, M. F., Cutri, R. M., Stiening, R., et al. 2006, *AJ*, **131**, 1163
- Smith, R. C. & MCELS Team 1998, *PASA*, **15**, 163
- Solomon, P. M., Rivolo, A. R., Barrett, J., & Yahil, A. 1987, *ApJ*, **319**, 730
- Trotta, R. 2008, *ConPh*, **49**, 71
- Ulrich, R. K. 1976, *ApJ*, **210**, 377
- van der Tak, F. F. S., Black, J. H., Schöier, F. L., Jansen, D. J., & van Dishoeck, E. F. 2007, *A&A*, **468**, 627
- Virtanen, P., Gommers, R., Oliphant, T. E., et al. 2020, *NatMe*, **17**, 261
- Wang, J., Zhang, Z., & Shi, Y. 2011, *MNRAS*, **416**, L21
- Whitney, B. A., Sewilo, M., Indebetouw, R., et al. 2008, *AJ*, **136**, 18
- Williams, J. P., de Geus, E. J., & Blitz, L. 1994, *ApJ*, **428**, 693
- Wong, T., Hughes, A., Ott, J., et al. 2011, *ApJS*, **197**, 16
- Wong, T., Hughes, A., Tokuda, K., et al. 2019, *ApJ*, **885**, 50
- Wünsch, R., Jáchym, P., Sidorin, V., et al. 2012, *A&A*, **539**, A116
- Yamaguchi, R., Mizuno, N., Mizuno, A., et al. 2001, *PASJ*, **53**, 985
- Zhang, Z.-Y., Gao, Y., Henkel, C., et al. 2014, *ApJL*, **784**, L31